



Cite this: *RSC Adv.*, 2025, **15**, 39071

## First-principles investigation of structural, electronic, optical, mechanical, and phonon properties of Pb- and Sn-based cubic oxide perovskites for optoelectronic applications

Md. Sakib Hasan Saikot,<sup>a</sup> Rifat Rafiu,<sup>a</sup> Imtiaz Ahamed Apon,<sup>b</sup> Ali El-Rayyes,<sup>c</sup> Md. Azizur Rahman,<sup>d</sup> Mohd Shkir,<sup>ef</sup> Zubair Ahmad<sup>gh</sup> and R. Marnadu<sup>i</sup>

This study presents a comprehensive first-principles investigation of Pb- and Sn-based cubic perovskites ( $\text{TiPbO}_3$ ,  $\text{TiSnO}_3$ ,  $\text{ZrPbO}_3$ , and  $\text{ZrSnO}_3$ ) using DFT within GGA-PBE and *m*GGA-rSCAN frameworks. Structural analysis confirms thermodynamic and structural stability for all compounds, with  $\text{ZrPbO}_3$  showing the lowest formation energy. Electronic band structure results reveal semiconducting behavior for  $\text{TiPbO}_3$  (1.996 eV),  $\text{TiSnO}_3$  (1.133 eV), and  $\text{ZrPbO}_3$  (2.349 eV), making them suitable for visible-light photovoltaics and photodetectors. In contrast,  $\text{ZrSnO}_3$ , due to its metallic behavior, could be useful as a conductive layer or as an electrode in optoelectronic devices. Optical analysis highlights strong absorption in the visible region for  $\text{TiSnO}_3$  and  $\text{ZrPbO}_3$ , while  $\text{ZrSnO}_3$  shows exceptional UV absorption ( $6.5 \times 10^5 \text{ cm}^{-1}$ ), suitable for UV shielding and plasmonic devices. High dielectric constants and low reflectivity further support optoelectronic and coating applications. Mechanical properties show  $\text{TiSnO}_3$  and  $\text{ZrPbO}_3$  possess high stiffness and ductility, ideal for flexible devices, while  $\text{TiPbO}_3$ 's anisotropy suits directional applications such as piezoelectric.  $\text{ZrSnO}_3$  is mechanically and dynamically unstable, limiting its immediate applicability. Anisotropy and phonon analyses confirm  $\text{TiPbO}_3$  and  $\text{ZrPbO}_3$  as mechanically and dynamically robust materials. Overall,  $\text{TiSnO}_3$ ,  $\text{TiPbO}_3$ , and  $\text{ZrPbO}_3$  emerge as promising multifunctional candidates for optoelectronic, energy, and stress-sensitive applications.

Received 17th August 2025

Accepted 6th October 2025

DOI: 10.1039/d5ra06065f

rsc.li/rsc-advances

### 1 Introduction

Over the past few decades, the field of optoelectronics and photovoltaic technologies has undergone significant advancements, driven in part by the development of oxide-based perovskite materials. These compounds have attracted

considerable attention due to their highly adaptable crystal structure, which can accommodate diverse elemental compositions and enable tunable electronic, optical, and structural properties. The intrinsic flexibility of the perovskite lattice makes it an ideal platform for designing next-generation functional materials for high-efficiency solar cells and other optoelectronic applications.<sup>1–3</sup>

Oxide perovskites, characterized by the general formula  $\text{ABO}_3$ , have particularly garnered attention for their unique electronic, optical, and structural attributes, making them indispensable in modern material science and device engineering. Recent advancements in material synthesis and characterization have further expanded the scope of oxide perovskites in optoelectronics.<sup>4</sup> Their wide bandgap, high dielectric constant, and defect tolerance make them suitable for applications ranging from light-emitting diodes (LEDs) to photodetectors.<sup>5</sup> Moreover, the environmental stability and nontoxicity of certain oxide perovskites position them as sustainable alternatives to traditional semiconductors in the quest for greener technologies.<sup>6,7</sup> Perovskites have been extensively studied over the centuries, with their first identification by Gustav Rose in 1839. Industrial investigations of perovskite oxides start focusing on the structural properties of  $\text{CaTiO}_3$ .

<sup>a</sup>Department of Material Science and Engineering, Khulna University of Engineering & Technology (KUET), Khulna 9203, Bangladesh

<sup>b</sup>Department of Electrical and Electronic Engineering, Bangladesh Army University of Science and Technology (BAUST), Saidpur 5311, Bangladesh

<sup>c</sup>Center for Scientific Research and Entrepreneurship, Northern Border University, 73213, Saudi Arabia

<sup>d</sup>Department of Electrical and Electronic Engineering, Begum Rokeya University, Rangpur, 5400, Bangladesh. E-mail: azizurrahmanatik49@gmail.com

<sup>e</sup>Department of Physics, College of Science, King Khalid University, Post Box 960, Abha, 61421, Saudi Arabia

<sup>f</sup>Smart Nano-Materials for Energy and Optoelectronic Devices Lab, Central Labs, King Khalid University, PO BOX 960, AlQura'a, Abha, 61421, Saudi Arabia

<sup>g</sup>Centre of Bee Research and its Products, King Khalid University, P. O. Box 9004, Abha 61413, Saudi Arabia

<sup>h</sup>Central Labs, King Khalid University, AlQura'a, P. O. Box 960, Abha, Saudi Arabia

<sup>i</sup>Department of Condensed Matter Physics, Saveetha School of Engineering, Saveetha Institute of Medical and Technical Sciences, SIMATS, Chennai, Tamil Nadu, 602 105, India



**BaTiO<sub>3</sub>** emerged as a key material for military and industrial applications, fulfilling the demand for advanced ferroelectric materials.<sup>8</sup> A DFT-based *ab initio* study of VGaO<sub>3</sub> and NbGaO<sub>3</sub> examines their structural, electronic, and optical properties. Using FP-LAPW with PBE-GGA and LDA + *U*, the indirect band gaps are determined as 0.45 eV for VGaO<sub>3</sub> and 0.51 eV for NbGaO<sub>3</sub>, confirming their semiconductor nature.<sup>9</sup> Optical analysis reveals that NbGaO<sub>3</sub> has superior properties, making it more suitable for optoelectronic applications.<sup>10</sup> ATaO<sub>3</sub> (A = Rb, Fr) perovskite oxides are gaining interest for their tailored electronic properties and strong optical response.<sup>11</sup> Recent research has explored various structural, electronic, and optical characteristics of perovskites. Taib *et al.*<sup>12</sup> analyzed BaTiO<sub>3</sub> and BaFeO<sub>3</sub> using the LDA + *U* approach. Liu *et al.* studied doping and structural traits of BaSnO<sub>3</sub> and SrSnO<sub>3</sub>.<sup>13</sup> Yaseen *et al.* focused on LaAlO<sub>3</sub>, evaluating its optical, electronic, and thermoelectric properties using the FP-LAPW technique.<sup>14</sup> Similarly, Babu *et al.* employed the mBJ-GGA approximation to examine the optoelectronic properties of cubic LaGaO<sub>3</sub> *via* WIEN2k software.<sup>15,16</sup> Other studies have addressed perovskites with diverse computational methods. Yaakob *et al.* investigated BiVO<sub>3</sub>'s structural properties and magnetic transitions using the LDA + *U* method in CASTEP, while Ekuma *et al.*<sup>17</sup> used GGA and the linear combination of atomic orbitals (LCAO) method to examine SrTiO<sub>3</sub>. Ali *et al.*<sup>18</sup> calculated the structural, optical, and electronic constraints of cubic SrVO<sub>3</sub> using the CASTEP code, while Hossain *et al.* studied SrVO<sub>3</sub>, BaVO<sub>3</sub>, PbVO<sub>3</sub>, and CaVO<sub>3</sub> using DFT for a comprehensive analysis of their physical

properties.<sup>19,20</sup> Kandy *et al.* explored SnAlO<sub>3</sub>'s thermoelectric and magnetoelectric behavior *via* WIEN2k, employing methods such as GGA, GGA + *U*, GGA + *U* + SOC, and mBJ. Roknuzzaman *et al.* analyzed Pb-free perovskites CsBX<sub>3</sub> (B = Sn, Ge; X = I, Cl, Br) for potential solar cell applications.<sup>21</sup> Musa Saad H.-E. studied the optoelectronic features of vanadium-based double perovskite.<sup>22</sup> Wang *et al.* examined ZnSnO<sub>3</sub>'s structural and optical traits using GGA,<sup>23</sup> while Kuma *et al.* evaluated SnTiO<sub>3</sub> and PbTiO<sub>3</sub> for their lattice dynamics, elastic properties, and electronic structure.<sup>24</sup> Hussain *et al.* further described the structural and optoelectronic behavior of transition-metal oxide perovskites.<sup>25</sup>

This study employs first-principles calculations based on the GGA-PBE and *meta*-GGA (*m*GGA) functionals within the CASTEP framework to investigate the structural, electronic, optical, and mechanical properties of novel ZDO<sub>3</sub> perovskites, where Z = Ti, Zr, and D = Pb, Sn. The analysis includes evaluations of the density of states, spin polarization effects, charge density distribution, elastic and anisotropic behavior, and electronic population characteristics. A systematic approach is adopted to understand how cation substitution at the A and B sites influences key material properties, such as lattice parameters, bandgap energies, optical response, spin-dependent electronic structure, and mechanical stability. These insights contribute to the advancement of stable, high-performance, and semiconductor materials for next-generation photovoltaic and optoelectronic applications.

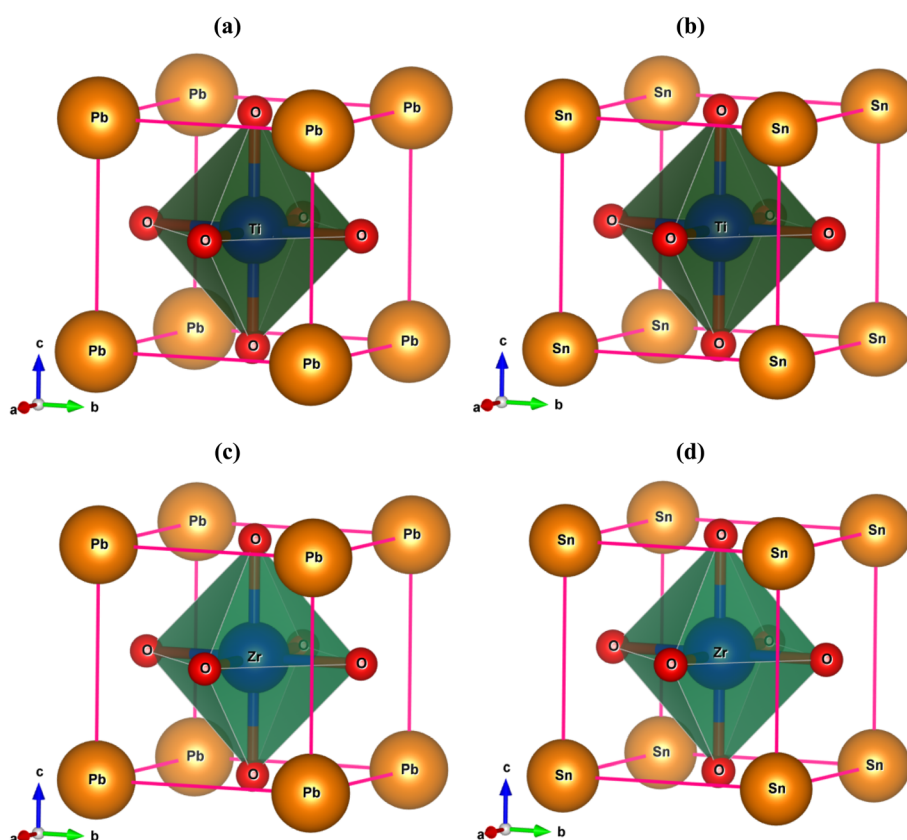


Fig. 1 Crystal structure of (a and b) TiDO<sub>3</sub> (D = Pb, Sn), and (c and d) ZrDO<sub>3</sub> (D = Pb, Sn).



## 2 Computational method

The Cambridge Serial Total Energy Package (CASTEP), based on Density Functional Theory (DFT), was utilized to investigate the structural, electronic, density of state, spin polarization effect, optical, charge density, mechanical properties, anisotropic, and population analysis of  $Z\text{DO}_3$  perovskites ( $Z = \text{Ti, Zr}$ ;  $D = \text{Pb, Sn}$ ). CASTEP is well-regarded for its accuracy and computational efficiency,<sup>26</sup> making it highly suitable for modeling the complex behaviors of advanced materials.<sup>27</sup> To treat exchange-correlation interactions, the Generalized Gradient Approximation (GGA) with the Perdew–Burke–Ernzerhof (PBE) functional was employed, offering a balanced trade-off between precision and computational cost.<sup>28–32</sup> Electron-ion interactions were modeled using Vanderbilt-type ultrasoft pseudopotentials. A plane-wave energy cutoff of 600 eV was adopted, ensuring convergence and stability in total energy and structural optimization, as illustrated in Fig. 1. The Brillouin zone was sampled using a dense Monkhorst–Pack grid of  $8 \times 8 \times 8$   $k$ -points to ensure accurate total energy calculations and convergence. Geometry optimizations were performed using the Broyden–Fletcher–Goldfarb–Shanno (BFGS) minimization algorithm under stringent convergence criteria. Mechanical properties were determined using the finite strain method implemented in the CASTEP module, in which small deformations are applied to extract the elastic constants from the resulting stress tensors.<sup>33</sup> The elastic anisotropy of  $Z\text{DO}_3$  ( $Z = \text{Ti, Zr}$ ;  $D = \text{Pb, Sn}$ ) perovskites was evaluated using the ELATE online tool, which computed anisotropic indices and visualized directional dependencies of Young's modulus, shear modulus, and Poisson's ratio based on the elastic tensor.<sup>34</sup> Optical properties, such as absorption spectra, reflectivity, and refractive indices, were calculated from the frequency-dependent dielectric function. Spin polarization effects and charge density distributions were also evaluated to gain deeper insight into electronic behavior. Electronic band structures and density of states (DOS) were analyzed to characterize the valence and conduction band

edges, which are critical for evaluating potential optoelectronic performance. This comprehensive methodology enabled precise characterization of  $\text{TiPbO}_3$ ,  $\text{TiSnO}_3$ ,  $\text{ZrPbO}_3$ , and  $\text{ZrSnO}_3$ , ensuring a reliable understanding of their structural, mechanical, and electronic behavior. Where available, results were compared with experimental data to validate the theoretical findings and confirm the materials' suitability for advanced technological applications, particularly in photovoltaics and optoelectronics.

## 3 Results & discussion

### 3.1. Structural properties

The compounds  $Z\text{DO}_3$ , where  $Z$  represents smaller cations such as Ti or Zr, and D includes larger cations like Pb or Sn, which exhibit a perovskite crystal structure with its characteristic cubic symmetry and the space group  $Pm\bar{3}m$  with an international space group number 221, are particularly well-defined for their high degree of structural orientation and versatility.<sup>35</sup> The crystal structure of the  $Z\text{DO}_3$  perovskite materials is illustrated in Fig. 1. In this structure, the  $Z$  atom, positioned at the 1b Wyckoff sites  $(1/2, 1/2, 1/2)$ , sits at the center of the cube and forms the core of the octahedral coordination with oxygen, which helps determine the electronic band structure and contributes significantly to its magnetic and optoelectronic behaviors.<sup>36</sup> The D atom is located at the 1a Wyckoff positions with coordinates  $(0, 0, 0)$  occupying the corners of the cubic unit cell. This placement provides overall stability and the dielectric property of the crystal by balancing the interaction with other atoms.<sup>37</sup> The oxygen (O) atoms themselves are arranged at the 3c Wyckoff positions  $(0, \frac{1}{2}, \frac{1}{2})$ , defining the face-centered positions that complete the three-dimensional connectivity of the lattice. This crystal structure has extensive applications in conversion and storage devices, including photovoltaic cells, capacitors, and piezoelectric sensors.

Finally, all the studied  $Z\text{DO}_3$  compounds maintain a cubic perovskite structure with well-defined structural symmetry, stability, and three-dimensional lattice connectivity.

**Table 1** The lattice parameter (Å), energy band gap (eV), unit cell volume (Å<sup>3</sup>), formation energy ( $\Delta E_f$ ), tolerance factor ( $t$ ) and physical nature of  $Z\text{DO}_3$  ( $Z = \text{Ti, Zr}$ , and  $B = \text{Pb, Sn}$ ) using different functionals

References	Compounds	Band gap, eV	Lattice constants (Å)	Density (g cm <sup>-3</sup> )	Volume $V$ (Å <sup>3</sup> )	Formation energy, $\Delta E_f$	Tolerance factor ( $t$ )	Function
This work	$\text{TiPbO}_3$	1.675	3.973	8.022	62.736	−3.767	1.027	GGA-PBE
	$\text{TiSnO}_3$	1.134	3.953	5.767	61.777	−3.738	0.915	
	$\text{ZrPbO}_3$	2.294	4.192	7.803	73.712	−3.878	0.975	
	$\text{ZrSnO}_3$	0	4.079	6.011	67.868	−3.142	0.864	
	$\text{TiPbO}_3$	2.300	3.843	8.098	62.144	—		m-GGA
	$\text{TiSnO}_3$	1.282	3.933	5.816	61.259	—		
	$\text{ZrPbO}_3$	2.815	4.162	7.878	72.095	—		
	$\text{ZrSnO}_3$	0	4.037	6.103	66.868	—		
	$\text{TiPbO}_3$	3.135	3.976	8.024	62.716	—		Hybrid-HSE06
	$\text{TiSnO}_3$	1.699	3.953	5.767	61.777	—		
38	$\text{ZrPbO}_3$	3.101	4.192	7.803	73.714	—		
	$\text{ZrSnO}_3$	0	4.080	6.107	67.869	—		
	$\text{TiSnO}_3$	1.670	—	—	—	—		GGA-PBE
	$\text{ThBeO}_3$	2.761	—	—	—	—		GGA-PBE



Table 1 presents a comprehensive comparison of the structural and electronic properties of the four  $Z\text{DO}_3$  perovskite compounds ( $\text{TiPbO}_3$ ,  $\text{TiSnO}_3$ ,  $\text{ZrPbO}_3$ , and  $\text{ZrSnO}_3$ ) calculated using GGA-PBE, *m*GGA-rSCAN, and the hybrid functional HSE06. The calculated lattice constants for the studied  $Z\text{DO}_3$  perovskites show only small variations across the employed exchange-correlation functionals. For instance,  $\text{TiPbO}_3$  exhibits values of 3.973 Å (GGA-PBE), 3.843 Å (*m*-GGA), and 3.976 Å (HSE06), while  $\text{TiSnO}_3$  remains nearly unchanged at  $\sim$ 3.95 Å for all functionals. Similarly,  $\text{ZrPbO}_3$  varies between 4.192 Å (PBE, HSE06) and 4.162 Å (*m*-GGA), whereas  $\text{ZrSnO}_3$  lies around 4.08 Å (PBE, HSE06) and 4.037 Å (*m*-GGA). These values indicate that hybrid HSE06 and GGA-PBE generally predict slightly larger lattice constants compared to *m*-GGA. The calculated densities exhibit a consistent trend with the variation in lattice parameters, as larger lattice constants correspond to lower densities.  $\text{TiPbO}_3$  has densities of 8.022 g cm<sup>-3</sup> (PBE), 8.098 g cm<sup>-3</sup> (*m*-GGA), and 8.024 g cm<sup>-3</sup> (HSE06), while  $\text{TiSnO}_3$  remains around  $\sim$ 5.8 g cm<sup>-3</sup> across all three functionals.  $\text{ZrPbO}_3$  is stable at  $\sim$ 7.8 g cm<sup>-3</sup>, whereas  $\text{ZrSnO}_3$  maintains  $\sim$ 6.0 g cm<sup>-3</sup> irrespective of functional. Thus, density variations are minimal, reflecting the consistency of structural stability predictions.

The formation energies ( $\Delta E_f$ ) confirm the thermodynamic stability of all studied compounds, with negative values across the board. Among them,  $\text{ZrPbO}_3$  shows the lowest energy ( $-3.878$  eV with PBE), followed by  $\text{TiPbO}_3$  ( $-3.767$  eV),  $\text{TiSnO}_3$  ( $-3.738$  eV), and  $\text{ZrSnO}_3$  ( $-3.142$  eV). This indicates that  $\text{ZrPbO}_3$  is the most stable, while  $\text{ZrSnO}_3$  is relatively less favorable energetically. In contrast, when the Z-site cation is substituted from Ti to Zr, an increasing trend in volume is observed, consistent with the larger ionic radius of Zr compared to Ti. The following formula can be used to determine the formation enthalpy,

$$\Delta E_f = E_{\text{tot}}(\text{ZDO}_3) - (E_Z + E_D + 3E_O) \quad (1)$$

where  $E_{\text{tot}}$  is the total energy of the relaxed  $\text{ZDO}_3$  structure obtained from DFT,  $E_S$  (Z) and  $E_S$  (D) are the standard reference energies of elements (Z = Ti, Zr) and (D = Pb, Sn) in their most stable forms, and  $E_S$  (O) is the energy of oxygen in its ground state. The factor N normalizes the energy to a per-formula-unit basis. If  $\Delta E_f < 0 \rightarrow$  the compound is thermodynamically stable, meaning it is energetically favorable to form from its constituent elements. If  $\Delta E_f > 0 \rightarrow$  the compound is unstable, and it would tend to decompose back into its elemental or competing phases. In Table 1 for  $\text{ZDO}_3$  ( $\text{TiPbO}_3$ ,  $\text{TiSnO}_3$ ,  $\text{ZrPbO}_3$ ,  $\text{ZrSnO}_3$ ), all  $\Delta E_f$  values are negative, which clearly indicates that these perovskites are stable against decomposition. In comparison to previous studies, the present work reports a band gap of 1.134 eV for  $\text{TiSnO}_3$  under PBE, which is slightly lower than the 1.670 eV value earlier reported using the same functional.<sup>38</sup> Similarly,  $\text{ThBeO}_3$  was reported with a band gap of 2.761 eV using GGA-PBE,<sup>39</sup> consistent with the general underestimation of band gaps by semi-local functionals compared to hybrid HSE06. The tolerance factor ( $t$ ), proposed by Goldschmidt, serves as a fundamental geometric criterion to predict the

stability and structural distortions in perovskite-type oxides. It is calculated using the relation,

$$t = \frac{r_A + r_X}{\sqrt{2}(r_B + r_X)} \quad (2)$$

For perovskite structures, the ideal range of the Goldschmidt tolerance factor ( $t$ ) lies between 0.8 and 1.0. Structures with  $t$  values between 0.8 and 0.9 are generally considered stable, while those in the range of 0.9 to 1.0 are regarded as more structurally stable or even super-stable, indicating a better fit between the ionic radii and a higher likelihood of forming a robust perovskite phase.<sup>34</sup> The calculated Goldschmidt tolerance factor for  $\text{ZrSnO}_3$ , as shown in Table 1, is 0.864, which lies within the generally accepted stability range of 0.8–0.9 for perovskite structures. This suggests that  $\text{ZrSnO}_3$  is structurally stable and likely to adopt a stable perovskite lattice. For the other compounds, the tolerance factors are 1.027 for  $\text{TiPbO}_3$ , 0.915 for  $\text{TiSnO}_3$ , and 0.975 for  $\text{ZrPbO}_3$ , all of which fall within the 0.9–1.0 range. These values indicate a higher degree of structural stability, implying that these materials have a strong tendency to form well-ordered and robust perovskite phases. Therefore, all the studied materials can be considered structurally stable perovskites.

### 3.2. Electrical properties

Investigating the electronic properties of a material is essential for understanding its conductivity and suitability for optoelectronic applications. The band structure in Fig. 2–4 illustrates how electron energy varies with momentum within the first Brillouin zone, offering key insights into both electronic and optical behavior. A critical parameter is the band gap, the energy difference between the valence band maximum (VBM) and conduction band minimum (CBM), which determines whether a material behaves as a metal, semiconductor, or insulator.<sup>40,41</sup> Fig. 2–4 present the electronic band structures of the  $\text{ZDO}_3$  perovskites calculated along the high-symmetry  $k$ -points path  $X-R-M-\Gamma-R$  using GGA-PBE (Fig. 2), *m*GGA-rSCAN (Fig. 3), and the hybrid functional HSE06 (Fig. 4). This approach was adopted to address the well-known underestimation of band gaps by semilocal functionals and to validate the electronic structures with a more accurate hybrid functional.

Fig. 2 present the electronic band structures of  $\text{ZDO}_3$  perovskites, calculated along the high-symmetry  $k$ -points path  $X-R-M-\Gamma-R$  using the GGA-PBE functional.  $\text{TiPbO}_3$  exhibits an indirect band gap of 1.675 eV, with the valence band maximum (VBM) located at the  $R$ -point and the conduction band minimum (CBM) at the  $\Gamma$ -point.

In contrast,  $\text{TiSnO}_3$  shows a smaller indirect band gap of 1.134 eV, where the VBM lies at the  $M$ -point and the CBM at the  $\Gamma$ -point.  $\text{ZrPbO}_3$  displays a larger indirect band gap of 2.294 eV ( $R-\Gamma$ ), whereas  $\text{ZrSnO}_3$  remains metallic with its valence and conduction bands overlapping near the Fermi level. Fig. 3, upon applying *m*GGA-rSCAN, the band gaps increase to 2.300 eV ( $\text{TiPbO}_3, R-\Gamma$ ), 1.282 eV ( $\text{TiSnO}_3, M-\Gamma$ ), and 2.815 eV ( $\text{ZrPbO}_3, R-\Gamma$ ).



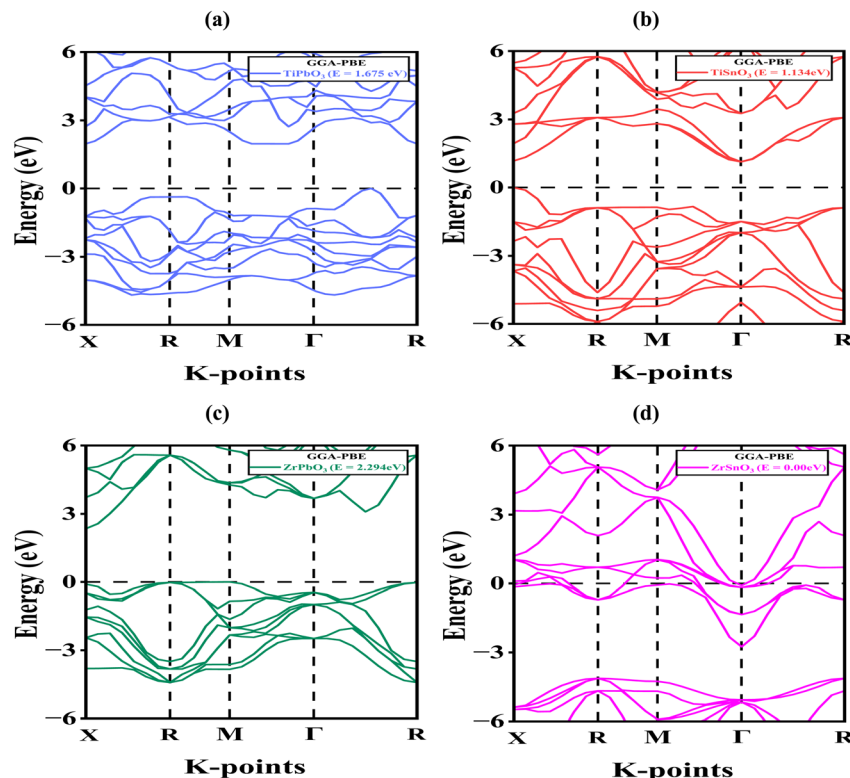


Fig. 2 Band structure of (a)  $\text{TiPbO}_3$ , (b)  $\text{TiSnO}_3$ , (c)  $\text{ZrPbO}_3$  and (d)  $\text{ZrSnO}_3$  using GGA-PBE function.

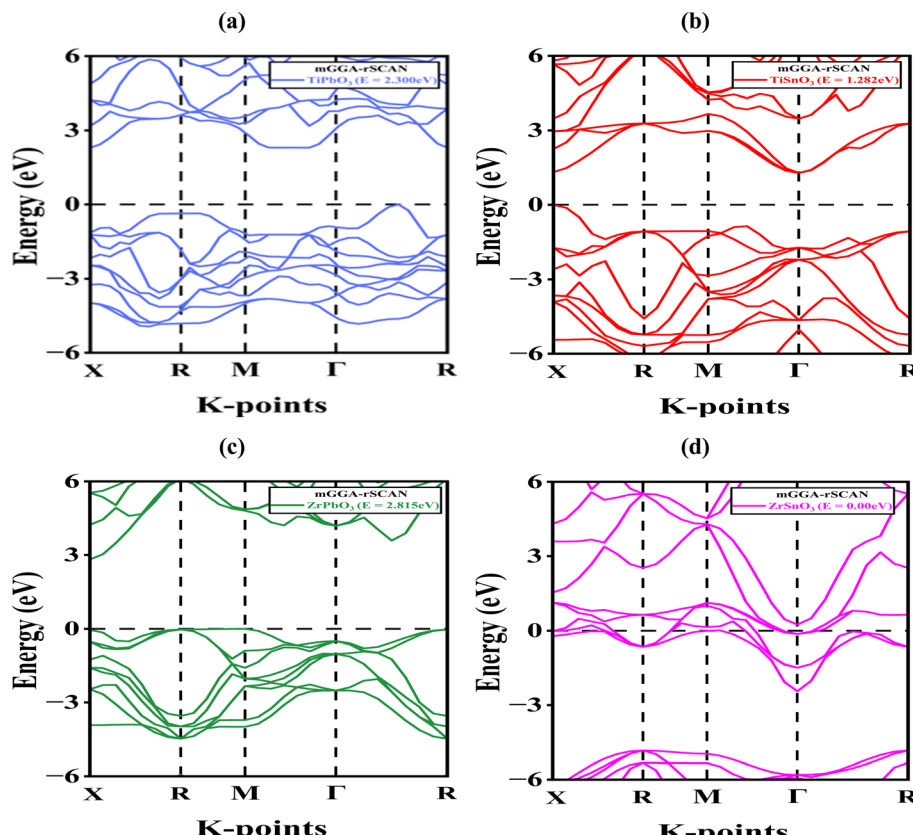


Fig. 3 Band structure of (a)  $\text{TiPbO}_3$ , (b)  $\text{TiSnO}_3$ , (c)  $\text{ZrPbO}_3$  and (d)  $\text{ZrSnO}_3$  using *m*GGA-rSCAN function.

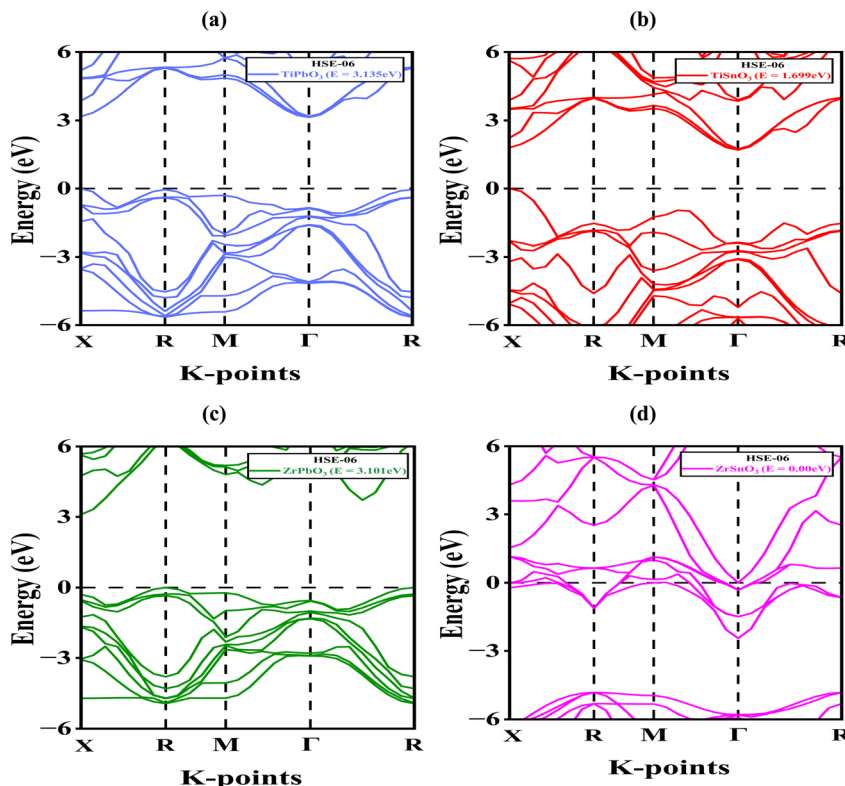


Fig. 4 Band structure of (a)  $\text{TiPbO}_3$ , (b)  $\text{TiSnO}_3$ , (c)  $\text{ZrPbO}_3$  and (d)  $\text{ZrSnO}_3$  using HSE-06 function.

$\Gamma$ ), while  $\text{ZrSnO}_3$  again shows metallic characteristics. To overcome the limitations of GGA and  $m$ GGA, we performed HSE06 calculations on the rSCAN-optimized structures (Fig. 4). The hybrid functional further corrects the underestimated gaps, yielding 3.135 eV for  $\text{TiPbO}_3$  ( $R-\Gamma$ ), 1.699 eV for  $\text{TiSnO}_3$  ( $M-\Gamma$ ), and 3.101 eV for  $\text{ZrPbO}_3$  ( $R-\Gamma$ ), while  $\text{ZrSnO}_3$  consistently retains metallicity.

Across all three functionals, the band gap trend follows  $\text{HSE06} > m\text{GGA-rSCAN} > \text{GGA-PBE}$ , and the dispersion along the  $X-R-M-\Gamma-R$  path confirms the indirect nature of the gaps in the semiconducting compounds, with  $\text{ZrSnO}_3$  remaining metallic. By including HSE06 calculations, the electronic structures and band gap values are now more quantitatively reliable. These results highlight the crucial role of exchange–correlation functionals in predicting electronic behavior and provide a validated framework for assessing the optoelectronic applicability of  $\text{ZDO}_3$  perovskites.

### 3.3. Density of states (DOS)

The Density of states (DOS) reflects the number of available electronic states per unit energy at each level, providing crucial insights into whether a material behaves as a metal, semiconductor, or insulator.<sup>42</sup> Fig. 5 presents the partial density of states (PDOS) of  $\text{TiPbO}_3$ ,  $\text{TiSnO}_3$ ,  $\text{ZrPbO}_3$ , and  $\text{ZrSnO}_3$ , showing how the atomic orbitals contribute to their electronic structures across the energy spectrum. The energy scale spans from  $-6$  eV to  $+6$  eV with the Fermi level ( $E_F$ ) at 0 eV, where the total DOS is plotted in red.

For all compounds, the valence band below  $E_F$  is dominated by O-2p orbitals, which exhibit strong hybridization with Ti-3d/ Zr-4d states and with Pb-6s/6p or Sn-5s/5p orbitals, indicating significant covalent character in the bonding. The conduction band above  $E_F$  is primarily governed by the Ti-3d or Zr-4d states, reflecting their central role in electronic excitations, while Pb and Sn orbitals provide secondary contributions. The presence of a band gap at the Fermi level in each system confirms their semiconducting behavior, with the size and sharpness of the band gap varying according to the D-site cation and the transition metal. Specifically, compounds containing Pb ( $\text{TiPbO}_3$  and  $\text{ZrPbO}_3$ ) show broader distributions in the valence region due to the involvement of Pb-6s and Pb-6p states, while Sn-based systems ( $\text{TiSnO}_3$  and  $\text{ZrSnO}_3$ ) display a more localized valence band structure dominated by O-2p and Sn-5p hybridization. Furthermore, substitution of Ti with Zr shifts the conduction band edge, reflecting differences in d-orbital localization between Ti-3d and Zr-4d, which in turn modifies the band gap width. These variations suggest that careful selection of cations (Pb vs. Sn, Ti vs. Zr) provides tunability of the electronic band structure, making these materials potentially suitable for diverse optoelectronic and energy-related applications.

### 3.4. Charge density analysis

Charge density analysis, derived from DFT calculations, reveals the distribution of electrons within a material. It helps distinguish bonding types. Covalent bonds show charge accumulation between atoms, while ionic bonds exhibit charge



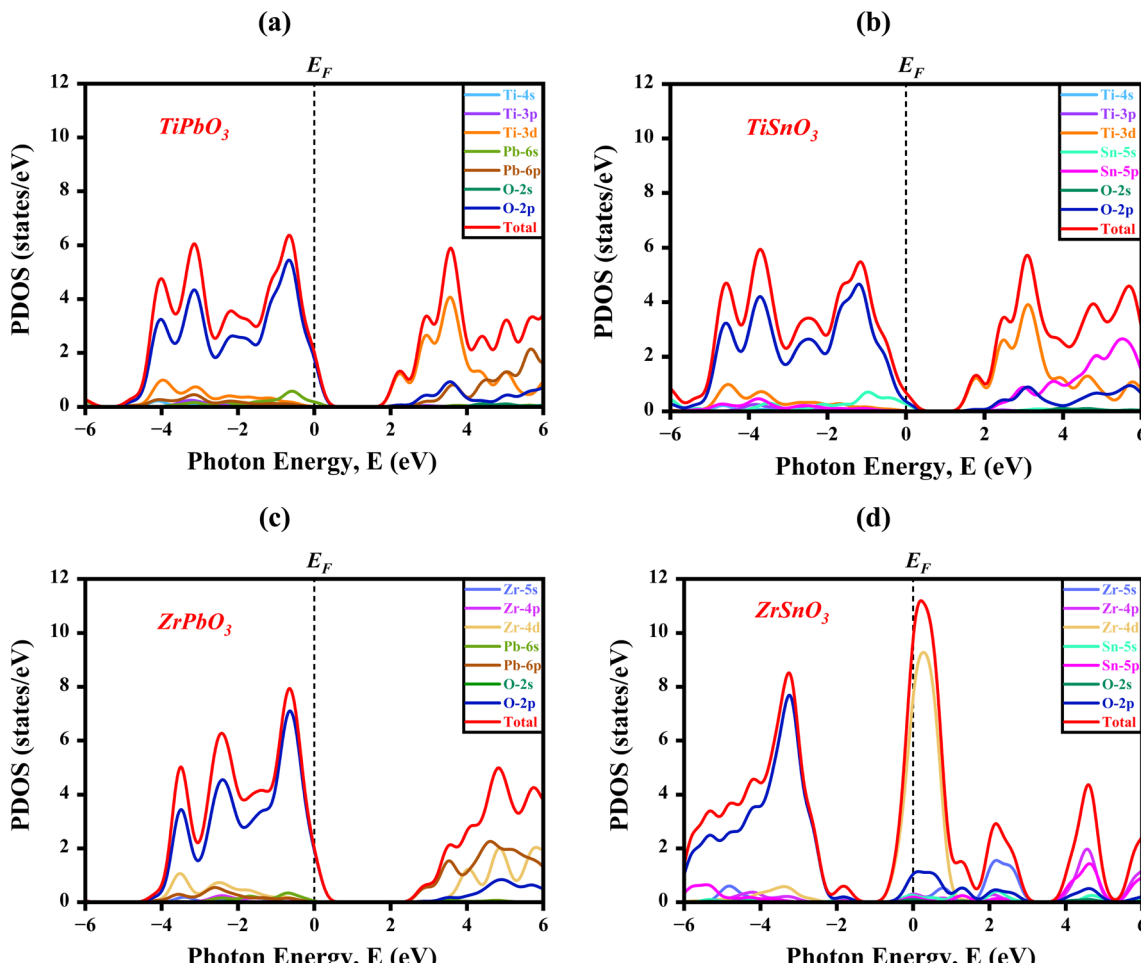


Fig. 5 Partial density of states (PDOS) for (a)  $\text{TiPbO}_3$ , (b)  $\text{TiSnO}_3$ , (c)  $\text{ZrPbO}_3$ , and (d)  $\text{ZrSnO}_3$ , showing the contributions of atomic orbitals to the valence and conduction bands.

separation.<sup>43</sup> The analysis also identifies regions of charge transfer and polarization, offering insights into bond strength and reactivity. It serves as a valuable complement to experimental techniques like X-ray diffraction and spectroscopy.<sup>44</sup> Fig. 6 shows Electron Density Difference (EDD) plots for four ZDO<sub>3</sub>-type perovskites:  $\text{TiSnO}_3$ ,  $\text{TiPbO}_3$ ,  $\text{ZrSnO}_3$ , and  $\text{ZrPbO}_3$ . These plots highlight charge accumulation and depletion regions within the crystal structure to evaluate bonding characteristics and electron localization. The color scale bars represent electron density differences, with red indicating charge accumulation and blue indicating depletion. In Fig. 6(a) for  $\text{TiSnO}_3$ , the maximum side-bar electron density reaches  $1.461 \times 10^1$ , showing strong charge localization around the central Ti and O atoms, forming Ti–O covalent bonds, while the surrounding Sn atoms show minimal accumulation, indicating weaker, more ionic Ti–Sn interactions at a greater distance.

In Fig. 6(b) for  $\text{TiPbO}_3$ , the charge intensity peaks at a higher value of  $2.539 \times 10^1$ , suggesting enhanced polarization and electron accumulation around Ti and O, forming strong Ti–O covalent bonds, while Pb atoms remain at lower density regions, implying weak long-range ionic Pb–O interactions. In Fig. 6(c) for  $\text{ZrSnO}_3$ , the maximum electron charge intensity is  $1.373 \times$

$10^1$ , with strong charge localization between Zr and O atoms, confirming robust Zr–O covalent bonding. The surrounding Sn atoms, being farther and appearing in low-density zones, again contribute to weaker Zr–Sn ionic interactions. Lastly, Fig. 6(d) for  $\text{ZrPbO}_3$  exhibits the highest intensity among the Zr-based systems electron charges intensity at  $2.372 \times 10^1$ , highlighting highly polarized Zr–O covalent bonds. The distant Pb atoms, surrounded by blue and green zones, imply negligible charge sharing and form weak ionic Pb–O bonds. Overall, the color gradients and maximum EDD values confirm that: Ti–O and Zr–O bonds are predominantly covalent due to high charge accumulation. Pb–O and Sn–O bonds are mostly ionic or weakly polar, with less charge overlap. Zr-based perovskites, especially  $\text{ZrPbO}_3$ , show stronger metal–oxygen interactions than Ti-based analogues due to higher electron localization intensity and more extensive red regions. This comparative EDD analysis provides crucial insight into the bonding nature and electronic structure modifications induced by B-site (Sn/Pb) substitutions.

### 3.5. Spin polarization effects

Spin-polarized DOS further separates spin-up and spin-down states, helping identify magnetic behavior.<sup>45</sup> This analysis is

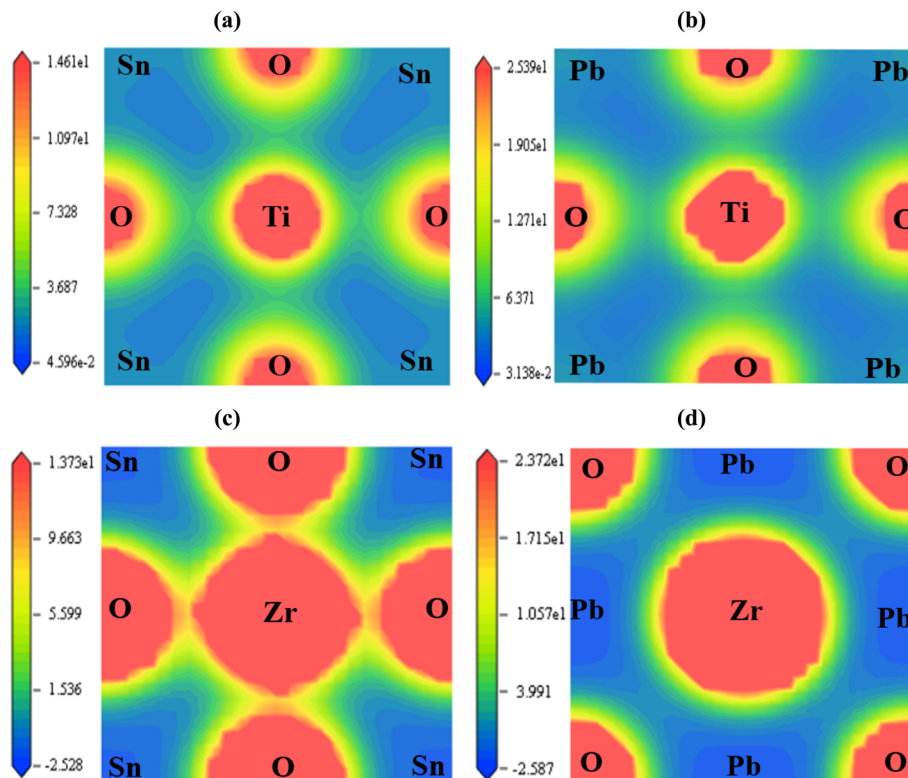


Fig. 6 Electron Density Difference (EDD) plots for (a)  $\text{TiSnO}_3$ , (b)  $\text{TiPbO}_3$ , (c)  $\text{ZrSnO}_3$ , and (d)  $\text{ZrPbO}_3$ -type perovskites, illustrating charge distribution and bonding characteristics.

crucial because it reveals whether a material is metallic, semiconducting, or insulating, and helps understand its magnetic, optical, and electronic properties. Thus, DOS is a fundamental tool in material design for applications like spintronics, photovoltaics, and magnetic storage. Fig. 7 presents the spin-polarized Total Density of States (TDOS) and Partial Density of States (PDOS) for four perovskite compounds— $\text{TiPbO}_3$ ,  $\text{TiSnO}_3$ ,  $\text{ZrPbO}_3$ , and  $\text{ZrSnO}_3$ —plotted against photon energy ( $E$ ) in the range of  $-20$  eV to  $+40$  eV, with the Fermi level ( $E_F$ ) set at  $0$  eV. In  $\text{TiPbO}_3$  (Fig. 7(a and b)), pronounced spin asymmetry is observed, with TDOS peaks reaching  $9.6$  states per eV for spin-up near  $-14$  eV and  $5.2$  states per eV at  $E_F$ , confirming its semiconducting and magnetic nature. The PDOS reveals dominant Ti-3d and Pb-6p orbital contributions near the Fermi level, accompanied by significant O-2p and O-2s states within the valence region. In  $\text{TiSnO}_3$  (Fig. 7(c and d)) also displays semiconducting behavior, with states crossing  $E_F$  and TDOS peaks of  $\sim 6.8$  states per eV (spin-up) at  $-13$  eV and  $\sim 4.5$  states per eV near  $E_F$ ; the conduction region is mainly governed by Ti-3d and Sn-5p orbitals, accompanied by significant O-2p and O-2s states within the valence region. In  $\text{ZrPbO}_3$  (Fig. 7(e and f)) exhibits significant spin polarization, with TDOS values of  $\sim 9.8$  states per eV (spin-up) near  $-18$  eV and  $\sim 4$  states per eV at  $E_F$ , while PDOS analysis confirms Zr-4d and Pb-6p hybridization as the primary contributors, accompanied by significant O-2p and O-2s states within the valence region.

In  $\text{ZrSnO}_3$  (Fig. 7(g and h)) shows comparatively weaker but still noticeable spin asymmetry, with TDOS reaching  $\sim 5.5$  states

per eV near  $-15$  eV and  $\sim 2.5$  states per eV around  $E_F$ , indicating a metallic and weakly magnetic character dominated by Zr-4d and Sn-5p states near the Fermi level, accompanied by significant O-2p and O-2s states within the valence region. Overall, the four compounds exhibit a consistent trend in which O-2p and O-2s states dominate the valence band and strongly hybridize with the D-site d and Z-site p states. This hybridization underpins the semiconducting behavior of  $\text{TiPbO}_3$ ,  $\text{TiSnO}_3$ , and  $\text{ZrPbO}_3$ , whereas  $\text{ZrSnO}_3$  displays metallic characteristics, with these interactions also influencing the magnetic response near the Fermi level.

### 3.6. Optical properties

The optical properties of a material, how it interacts with light, are essential for both practical applications and scientific research. These properties encompass various parameters, including absorption, reflectivity, refractive index, dielectric function, optical conductivity, and energy loss function.<sup>46</sup> Together, they provide critical insights into a material's behavior under electromagnetic radiation. Understanding these characteristics is vital for optimizing material performance in advanced technologies and supports the development of scientific innovations across fields such as photonics, optoelectronics, and energy harvesting.

**3.6.1. Dielectric function.** The dielectric function describes how a material responds to an external electric field, particularly in terms of how it polarizes and how it interacts with electromagnetic waves like light. It is a complex function, usually written as:<sup>47</sup>



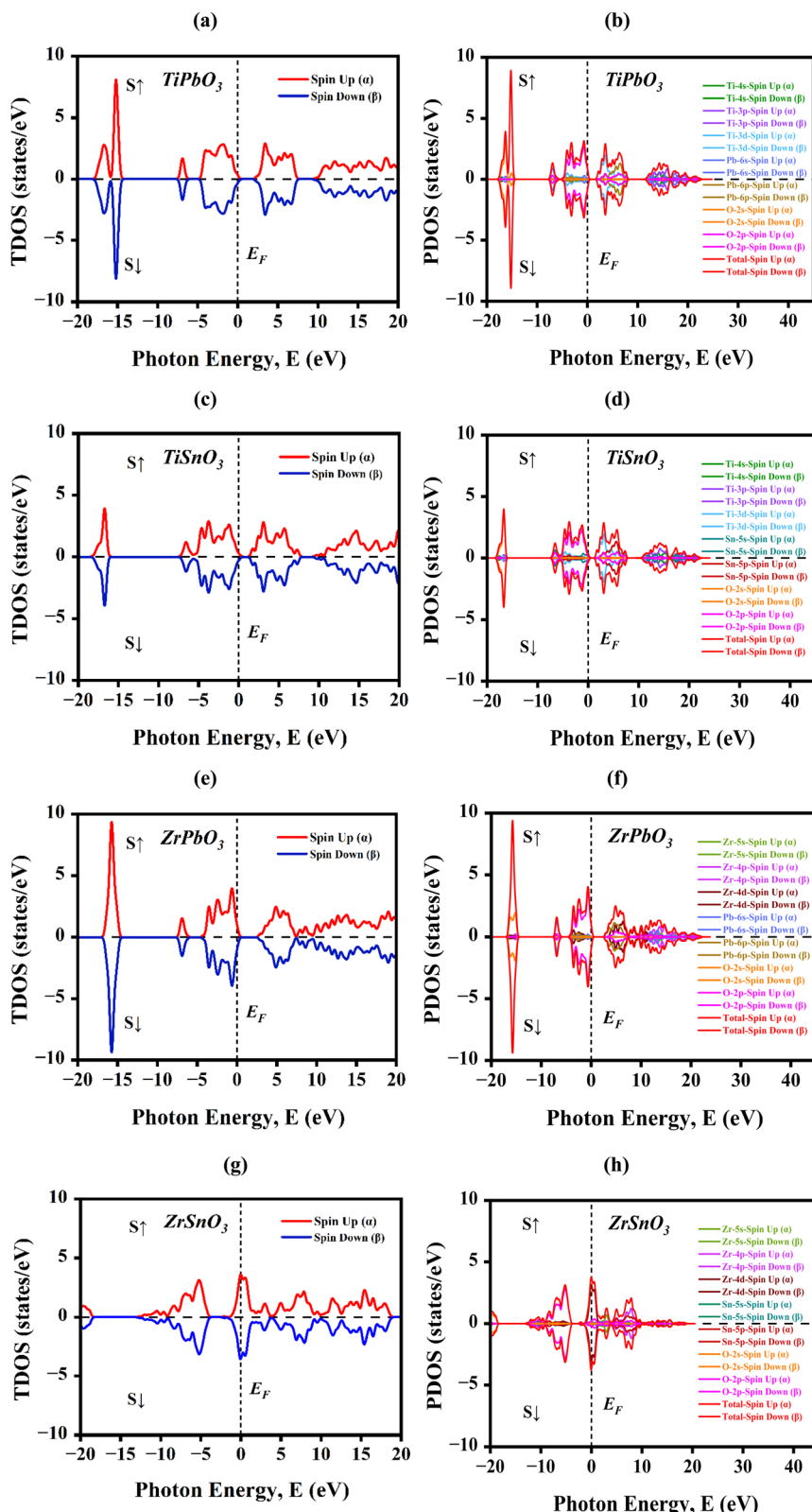


Fig. 7 Spin-up and spin-down electron density distribution in (a and b)  $TiPbO_3$ , (c and d)  $TiSnO_3$ , (e and f)  $ZrPbO_3$ , and (g and h)  $ZrSnO_3$  materials.

$$\varepsilon(\omega) = \varepsilon_1(\omega) + i\varepsilon_2(\omega) \quad (3)$$

where  $\varepsilon_1(\omega)$  is the real part (representing dispersion or polarization) and  $\varepsilon_2(\omega)$  is the imaginary part (representing absorption). The mathematical relation in the real and imaginary parts of the dielectric function can be described as,<sup>48</sup>

$$\varepsilon_1(\omega) = 1 + \frac{2}{\pi} P \int_0^\infty \frac{\omega'^{\varepsilon_2}(\omega')}{\omega'^2 - \omega^2} d\omega' \quad (4)$$

$$\varepsilon_2(\omega) = \frac{2e^2\pi}{\Omega\varepsilon_0} \sum_{KVC} \left| \langle \psi_k^c | U \cdot \vec{r} | \psi_k^V \rangle \right|^2 \delta(E_K^C - E_K^V - E) \quad (5)$$

where the dielectric function is split into its real part,  $\varepsilon_1(\omega)$ , and imaginary part,  $\varepsilon_2(\omega)$ , representing light absorption at frequency  $\omega$ . Here,  $e^2$  is the electronic charge squared,  $\pi$  is a constant,  $\Omega$  is the unit cell volume, and  $\varepsilon_0$  is the vacuum permittivity. The summation  $\sum(KVC)$  covers  $k$ -points in the Brillouin zone, capturing transitions from valence ( $V$ ) to conduction bands ( $C$ ). The matrix element  $\psi_k^c | U \cdot \vec{r} | \psi_k^V$ , involving position operator  $r$  and polarization vector  $U$ , gives the transition probability between the conduction state  $\psi_k^c$  and valence state  $\psi_k^V$ . The Dirac delta function,  $(E_K^C - E_K^V - E)$  ensures energy conservation in these electronic transitions, where  $E_K^C$  and  $E_K^V$  are conduction and valence band energies, respectively, at wave vector  $K$ , with  $E$  as photon energy.

Fig. 8(a) presents the dielectric function ( $\varepsilon$ ) as a function of photon energy for  $\text{TiPbO}_3$ ,  $\text{TiSnO}_3$ ,  $\text{ZrPbO}_3$ , and  $\text{ZrSnO}_3$ , showcasing both the real and imaginary components across the 0 to 16 eV energy range, which includes the infrared (IR), visible, and ultraviolet (UV) regions, marked by a vertical color strip. At zero frequency, the real part of the dielectric function,  $\varepsilon_1(0)$ , reflects the material's static electronic polarizability. For  $\text{TiPbO}_3$ ,  $\text{TiSnO}_3$ ,  $\text{ZrPbO}_3$ , and  $\text{ZrSnO}_3$ , the  $\varepsilon_1(0)$  values are 6.406, 9.607, 6.977, and above 20, respectively, indicating strong dielectric screening and suggesting the potential for high refractive index behavior. The dielectric curves begin at these static values and gradually decrease, reaching zero at photon energies of 6.88 eV, 5.50 eV, 6.278 eV, and 0.675 eV, respectively. The imaginary part ( $\varepsilon_2$ ), shown by lighter lines, captures energy losses due to interband transitions, with pronounced peaks in the visible to UV region for all compounds, especially  $\text{TiSnO}_3$  and  $\text{ZrPbO}_3$ . These trends imply that the dielectric properties are strongly dependent on the cationic composition, with the materials demonstrating promising characteristics for applications in optoelectronic, photonic, and dielectric-based devices.

**3.6.2. Absorption.** Absorption ( $\alpha$ ) is the process by which a material takes in light energy, often converting it into heat or exciting electrons to higher energy states. It plays a key role in determining how much light a material can capture, making it essential for applications like solar cells, photodetectors, and optical coatings.<sup>49</sup>

$$\alpha(\omega) = \sqrt{2\omega} \left[ \sqrt{\varepsilon_1^2(\omega) + \varepsilon_2^2(\omega)} - \varepsilon_1(\omega) \right]^{\frac{1}{2}} \quad (6)$$

Fig. 8(b) illustrates the variation of the absorption coefficient ( $\alpha$ ) as a function of photon energy for four perovskite oxides:  $\text{TiPbO}_3$ ,  $\text{TiSnO}_3$ ,  $\text{ZrPbO}_3$ , and  $\text{ZrSnO}_3$ . The photon energy spans from 0 to 16 eV, covering the infrared (IR), visible, and ultraviolet (UV) spectral regions, which are distinctly marked on the plot. All compounds exhibit increasing absorption with rising photon energy, showing multiple pronounced peaks in the UV region. Among the materials,  $\text{TiSnO}_3$  and  $\text{ZrPbO}_3$  demonstrate stronger absorption in the visible region compared to  $\text{TiPbO}_3$  and  $\text{ZrSnO}_3$ , suggesting better suitability for visible-light-driven applications. The inset highlights the low-energy region (0 to 2.5 eV), revealing that  $\text{TiSnO}_3$  possesses the earliest absorption onset, indicating the smallest optical band gap among the studied materials. These observations suggest that the optical absorption behavior of these compounds is strongly dependent on their cationic composition, with  $\text{TiSnO}_3$  standing out as a promising candidate for optoelectronic and photovoltaic applications.

**3.6.3. Conductivity.** Conductivity is a measure of a material's ability to allow the flow of electric current. It depends on the presence of free charge carriers (like electrons or ions), and materials with high conductivity, such as metals, are used in electrical wiring and electronic devices.

Optical conductivity is a complex quantity defined as:<sup>50</sup>

$$\sigma(\omega) = \sigma_1(\omega) + i\sigma_2(\omega) \quad (7)$$

Fig. 8(c) displays the optical conductivity ( $\sigma$ ) as a function of photon energy for  $\text{TiPbO}_3$ ,  $\text{TiSnO}_3$ ,  $\text{ZrPbO}_3$ , and  $\text{ZrSnO}_3$ , highlighting both the real and imaginary parts over the photon energy range of 0 to 16 eV, which spans the infrared (IR), visible, and ultraviolet (UV) regions marked by a vertical color band. The real part of the optical conductivity shows a similar trend to the absorption coefficient, as both are related to the material's interaction with incident photons. The imaginary part, shown with corresponding faded lines, fluctuates across positive and negative values, suggesting varying polarization response and interband transitions under the influence of an external electromagnetic field. Notably,  $\text{ZrPbO}_3$  and  $\text{TiSnO}_3$  exhibit higher real conductivity in the visible region, implying better performance in optoelectronic applications. Overall, the variation in optical conductivity with photon energy reflects the distinct electronic structures of these perovskites and their suitability for energy-harvesting and photonic device applications.

**3.6.4. Loss function.** The loss function, often denoted as  $L(\omega)$ , describes how much energy a fast-moving electron loses as it passes through a material due to interactions with the material's electrons. It is mathematically given by:<sup>51</sup>

$$L(\omega) = \frac{\varepsilon_2(\omega)}{\varepsilon_1^2(\omega) + \varepsilon_2^2(\omega)} \quad (8)$$

Fig. 8(d) presents the energy loss function  $L(\omega)$  as a function of photon energy (0 to 16 eV) for four perovskite compounds:  $\text{TiPbO}_3$ ,  $\text{TiSnO}_3$ ,  $\text{ZrPbO}_3$ , and  $\text{ZrSnO}_3$ . The x-axis covers the infrared (IR), visible, and ultraviolet (UV) spectral regions, with a color band indicating the visible range (1.50 to 3.5 eV). All



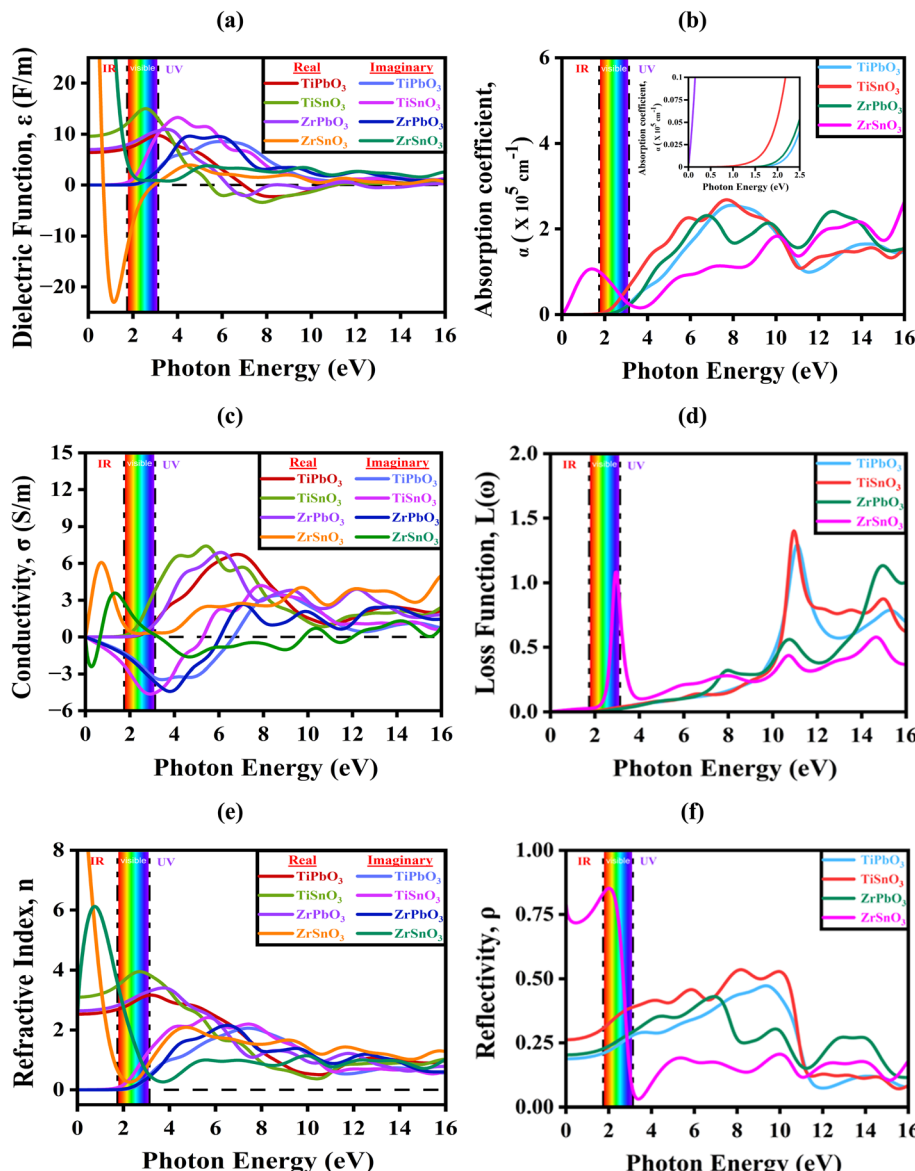


Fig. 8 Optical functions of (a) absorption coefficient, (b) conductivity, (c) dielectric function, (d) loss function, (e) refractive index (f) reflectivity of ZDO<sub>3</sub> perovskite materials.

materials exhibit low loss values in the visible region, suggesting minimal energy dissipation and good transparency, while pronounced peaks occur in the UV region, indicating strong plasmonic or interband transitions. TiPbO<sub>3</sub> and TiSnO<sub>3</sub> display sharper and higher peaks around 9.5 to 13 eV, whereas ZrPbO<sub>3</sub> shows a broader response near 12 eV, and ZrSnO<sub>3</sub> exhibits the weakest peaks, indicating lower energy loss. The presence of Pb and Ti tends to enhance the intensity and shift the peaks to higher energies compared to Sn and Zr-based counterparts. These results highlight the optical loss behavior and potential of these materials for UV-optical and plasmonic applications in optoelectronic and energy devices.

**3.6.5. Refractive index.** The refractive index ( $n$ ) is a measure of how much light slows down and bends when it enters a material from a vacuum or another medium. It is defined as:

$$n_1(\omega) = \left[ \frac{1}{2} \left( \sqrt{\varepsilon_1^2(\omega) + \varepsilon_2^2(\omega)} + \varepsilon_1(\omega) \right) \right]^{\frac{1}{2}} \quad (9)$$

$$n_2(\omega) = \left[ \frac{1}{2} \left( \sqrt{\varepsilon_1^2(\omega) + \varepsilon_2^2(\omega)} + \varepsilon_1(\omega) \right) \right]^{\frac{1}{2}} \quad (10)$$

where  $n_1(\omega)$  is the real part, and  $n_2(\omega)$  is the imaginary part.<sup>52</sup> The real part of the refractive index is the speed at which electromagnetic waves or light pass through the medium. It describes the phase velocity of light in a particular material. The imaginary part of the refractive index is also known as the extinction coefficient. It measures the quantity of electromagnetic waves absorbed as they pass through the material.

Fig. 8(e) illustrates the variation of the refractive index  $n$ , both real and imaginary parts, as a function of photon energy (0



to 16 eV) for four perovskite materials:  $\text{TiPbO}_3$ ,  $\text{TiSnO}_3$ ,  $\text{ZrPbO}_3$ , and  $\text{ZrSnO}_3$ . The spectral regions are marked as IR, visible, and UV, with the visible range (~1.65 to 3.1 eV) highlighted in a rainbow band. The real part of the refractive index, which indicates the phase velocity of light in the material, is shown by solid lines: red ( $\text{TiPbO}_3$ ), green ( $\text{TiSnO}_3$ ), purple ( $\text{ZrPbO}_3$ ), and orange ( $\text{ZrSnO}_3$ ). The imaginary part, which relates to the material's optical absorption, is shown by blue ( $\text{TiPbO}_3$ ), navy ( $\text{TiSnO}_3$ ), magenta ( $\text{ZrPbO}_3$ ), and cyan ( $\text{ZrSnO}_3$ ) lines. In the low-energy IR region, the real refractive index is high for all compounds, especially for  $\text{ZrSnO}_3$ , which peaks above 7. As photon energy increases, the real index gradually decreases for all materials and stabilizes around 1.5 to 2.5 in the UV region. The imaginary part (absorption) remains low in the visible range and rises in the UV, indicating that these materials are transparent in the visible region but absorb strongly in the UV. This behavior suggests these perovskites are promising for transparent optical coatings, photovoltaic devices, and UV filtering applications, where high refractive index and selective absorption are desirable.

**3.6.6. Reflectivity.** Reflectivity is the measure of how much light (or electromagnetic radiation) is reflected off the surface of a material rather than being absorbed or transmitted. It is usually expressed as a ratio or percentage:

$$R(\omega) = \left| \frac{\tilde{n}(\omega) - 1}{\tilde{n}(\omega) + 1} \right|^2 = \left| \frac{\sqrt{\varepsilon(\omega)} - 1}{\sqrt{\varepsilon(\omega)} + 1} \right|^2 \quad (11)$$

where  $R(\omega)$  is the frequency-dependent reflectivity,  $n(\omega)$  is the real part (refractive index),  $k(\omega)$  is the extinction coefficient, related to absorption, and  $\varepsilon_1$  and  $\varepsilon_2$  are the real and imaginary parts of the dielectric function. Fig. 8(f) illustrates the reflectivity ( $\rho$ ) as a function of photon energy (0 to 16 eV) for four perovskite compounds,  $\text{TiPbO}_3$ ,  $\text{TiSnO}_3$ ,  $\text{ZrPbO}_3$ , and  $\text{ZrSnO}_3$ , across the infrared (IR), visible, and ultraviolet (UV) spectral regions, with the visible range (~1.65 to 3.1 eV) highlighted in a rainbow band. In the IR region, all materials exhibit high reflectivity, especially  $\text{ZrSnO}_3$ , which peaks near 0.8, indicating strong reflection of low-energy photons. As photon energy increases into the visible region, reflectivity drops significantly for all materials, particularly for  $\text{ZrSnO}_3$  and  $\text{TiSnO}_3$ , suggesting good transparency and low optical loss in that range. In the UV region,  $\text{TiPbO}_3$  and  $\text{TiSnO}_3$  show moderate reflectivity peaks, while  $\text{ZrPbO}_3$  reflects strongly between 8 and 12 eV, and  $\text{ZrSnO}_3$  maintains the lowest reflectivity overall. These trends imply that these compounds, especially  $\text{ZrSnO}_3$ , are promising for applications requiring low reflectance in the visible range, such as solar cells, optical coatings, and transparent electronic devices.

### 3.7. Mechanical properties

The mechanical properties of a material, encompassing elastic stability, stiffness, ductility, hardness, and anisotropy, are primarily determined by its elastic constants. The characteristics of double perovskite materials were meticulously assessed using DFT, yielding values that provide essential insight into the compound's structural integrity and potential utility in diverse mechanical and electrical contexts. The primary elastic constants  $C_{11}$ ,  $C_{12}$ , and  $C_{44}$  were computed and are presented in Table 2. These constants indicate the material's resistance to deformation when subjected to applied stress. We utilized the Born stability criterion for cubic crystals to evaluate mechanical stability, which is articulated as follows:

$$C_{11} > 0, C_{44} > 0, C_{11} - C_{12} > 0 \text{ and } C_{11} + 2C_{12} > 0 \quad (12)$$

Mechanical stability of the materials was evaluated based on the Born stability criteria, as outlined in eqn (12). All the calculated elastic constants are positive and satisfy the corresponding Born stability criteria, confirming the mechanical stability of all the investigated compounds, except for  $\text{ZrSnO}_3$ , which shows a negative  $C_{44}$  value. The detailed mechanical parameters are presented in Table 2.

Table 2 presents the Cauchy pressure ( $C_p = C_{12} - C_{44}$ ) and shear constant ( $C_s = (C_{11} - C_{12})/2$ ) for four  $\text{ZDO}_3$  perovskites ( $\text{TiPbO}_3$ ,  $\text{TiSnO}_3$ ,  $\text{ZrPbO}_3$ ,  $\text{ZrSnO}_3$ ), compared to reference data for  $\text{SnTiO}_3$ .<sup>53</sup> These mechanical parameters are essential for evaluating the stability, ductility, brittleness, and bonding characteristics of materials. A positive Cauchy pressure ( $C_p$ ) typically indicates ductile behavior and metallic bonding, whereas a negative  $C_p$  suggests brittleness and directional covalent bonding.<sup>54</sup> The shear constant ( $C_s$ ) reflects resistance to shear deformation, thus representing mechanical robustness.<sup>55</sup> Among the studied compounds,  $\text{TiSnO}_3$  and  $\text{ZrPbO}_3$  exhibit the most favorable mechanical profiles, with  $C_p = 24.846$  GPa and  $C_s = 78.568$  GPa for  $\text{TiSnO}_3$ , and  $C_p = 23.013$  GPa and  $C_s = 100.652$  GPa for  $\text{ZrPbO}_3$ , indicating a good balance of ductility and stiffness.  $\text{TiPbO}_3$  also shows ductile behavior ( $C_p = 35.571$  GPa), but its lower  $C_s$  (46.648 GPa) suggests a comparatively softer nature. In contrast,  $\text{ZrSnO}_3$  exhibits a negative  $C_{44}$  (-83.419 GPa), resulting in an anomalously high and unphysical  $C_p$  value (151.178 GPa), indicating slightly brittle behavior and moderate shear resistance intermediate between the softer  $\text{TiPbO}_3$  and the stiffer  $\text{TiSnO}_3$  and  $\text{ZrPbO}_3$ .

The mechanical parameters, including bulk modulus ( $B$ ), shear modulus ( $G$ ), Young's modulus ( $E$ ), Poisson's ratio ( $\nu$ ),

**Table 2** Elastic stiffness constants ( $C_{ij}$ ), Cauchy pressure ( $C_p$ ), and shear constant of the  $\text{ZDO}_3$  ( $Z = \text{Ti}, \text{Zr}$ , and  $D = \text{Pb}, \text{Sn}$ ) perovskite compounds

Ref.	Compounds	$C_{11}$	$C_{12}$	$C_{44}$	$\zeta$	$C_p$	$C_s$
This work	$\text{TiPbO}_3$	160.159	66.862	31.291	0.553	128.868	46.648
	$\text{TiSnO}_3$	269.434	112.298	87.452	0.553	181.982	78.568
	$\text{ZrPbO}_3$	290.019	88.715	65.702	0.452	224.317	100.652
	$\text{ZrSnO}_3$	285.203	67.759	-83.419	0.388	368.622	108.722
	$\text{SnTiO}_3$	220.36	97.96	100.28	—	—	—



**Table 3** The Bulk Modulus ( $B$ ), shear modulus ( $G$ ), Young's Modulus ( $E$ ), Poisson's ratio ( $\nu$ ), and Pugh's ratio  $B/G$  of the compound of  $Z\text{DO}_3$  ( $Z = \text{Ti}$ ,  $\text{Zr}$  and  $\text{D} = \text{Pb}$ ,  $\text{Sn}$ )

Ref.	Compound	$B$	$G$	$E$	$\nu$	$B/G$	$H_V$	$\mu_M$
This work	$\text{TiPbO}_3$	60.514	40.424	99.186	0.226	1.496	7.981	1.933
	$\text{TiSnO}_3$	164.67	83.783	214.904	0.282	1.965	9.810	0.958
	$\text{ZrPbO}_3$	155.82	77.991	200.518	0.285	1.997	9.153	1.212
	$\text{ZrSnO}_3$	140.24	-145.591	-667.899	1.293	-0.963	9.961	0.078
53	$\text{SnTiO}_3$	138.76	82.26	206.07	—	1.68	—	—

Pugh's ratio ( $B/G$ ), Vickers hardness ( $H_V$ ), and machinability index ( $\mu_M$ ), are summarized in Table 3.<sup>56</sup> Here are some of the formulas we use to calculate these properties:

$$\text{Bulk Modulus, } B = \frac{C_{11} + 2C_{12}}{3} \quad (13)$$

$$\text{Shear modulus, } G = \frac{G_V + B_R}{2} \quad (14)$$

$$\text{Young's Modulus, } E = \frac{9BG}{3B + G} \quad (15)$$

$$\text{Pugh's Modulus, } B/G \quad (16)$$

$$A_2 = \frac{4C_{55}}{C_{22} + C_{33} - 2C_{23}} \quad (18)$$

$$A_3 = \frac{4C_{66}}{C_{11} + C_{22} - 2C_{12}} \quad (19)$$

Because of the cubic symmetry,

$$A_1 = A_2 = A_3 = \frac{4C_{44}}{C_{11} + C_{33} - 2C_{13}} = \frac{2C_{44}}{C_{11} - C_{13}} \quad (20)$$

The Zener isotropic factor  $A$  can be defined as,

$$A = \frac{2C_{44}}{C_{11} - C_{12}} \quad (21)$$

These quantities offer valuable insight into the mechanical stability, strength, ductility, and machinability of the studied compounds.<sup>40</sup> The bulk modulus ( $B$ ) measures a material's resistance to uniform compression, while the shear modulus ( $G$ ) reflects its resistance to shape deformation under shear stress. Young's modulus ( $E$ ) indicates overall stiffness. Poisson's ratio ( $\nu$ ) helps assess bonding characteristics, where values near 0.25 typically correspond to covalent bonding. Pugh's ratio ( $B/G$ ) is commonly used to classify materials as ductile ( $B/G > 1.75$ ) or brittle ( $B/G < 1.75$ ).<sup>57</sup> Vickers hardness ( $H_V$ ) estimates a material's resistance to plastic deformation, and the machinability index ( $\mu_M$ ) reflects ease of machining.

Among the investigated compounds,  $\text{TiSnO}_3$  exhibits the highest values of  $B$  (164.677 GPa),  $G$  (83.783 GPa), and  $E$  (214.904 GPa), suggesting excellent stiffness and elastic resistance. Its  $B/G$  ratio of 1.965 and Poisson's ratio of 0.282 point to good ductility and mixed metallic-covalent bonding.  $\text{ZrPbO}_3$  also displays strong mechanical performance, with  $B = 155.816$  GPa,  $G = 77.991$  GPa,  $E = 200.518$  GPa, and  $B/G = 1.997$ , indicating a favorable combination of strength and ductility.  $\text{TiPbO}_3$ , while softer ( $B = 60.514$  GPa,  $G = 40.424$  GPa), remains ductile ( $B/G = 1.496$ ), albeit to a lesser degree. Conversely,  $\text{ZrSnO}_3$  yields negative values for  $G$  and  $E$ , and an unphysically high Poisson's ratio (1.293), implying mechanical instability. For comparison, the reference compound  $\text{SnTiO}_3$ ,<sup>53</sup> shows  $B = 138.76$  GPa,  $G = 82.26$  GPa, and  $E = 206.07$  GPa, reflecting a mechanically strong and stable structure.

The subsequent formulas delineate the equations for the shear anisotropic components, the subsequent formulas delineate the equations for the shear anisotropic components,

$$A_1 = \frac{4C_{44}}{C_{11} + C_{33} - 2C_{13}} \quad (17)$$

For an isotropic material,  $A = A_1 = A_2 = A_3 = 1$ , and the variation from unity corresponds to the anisotropy of a material.<sup>58</sup>

The universal anisotropy index  $A^U$ , equivalent Zener anisotropy measure  $A^{\text{eq}}$ , anisotropy in compressibility  $A^B$ , and anisotropy in shear  $A_G$  can all be determined using the standard equations for any symmetry.<sup>59</sup>

$$A^U = \frac{B_V}{B_V} + 5 \frac{G_V}{B_R} - 6 \geq \quad (22)$$

$$A^B = \frac{B_V - B_R}{B_V + B_R} \quad (23)$$

$$A^{\text{eq}} = \left( 1 + \frac{5}{12} A^U \right) + \sqrt{\left( 1 + \frac{5}{12} A^U \right)^2 - 1} \quad (24)$$

$$A_G = \frac{G_V - G_R}{G_V + G_R} \quad (25)$$

Table 4 provides a comparative analysis of the different anisotropies of  $Z\text{DO}_3$  perovskites, revealing a striking diversity in performance across  $\text{TiPbO}_3$ ,  $\text{TiSnO}_3$ ,  $\text{ZrPbO}_3$ , and  $\text{ZrSnO}_3$ ,

**Table 4** Different anisotropy factors for  $Z\text{DO}_3$  ( $Z = \text{Ti}$ ,  $\text{Zr}$ , and  $\text{D} = \text{Pb}$ ,  $\text{Sn}$ ) perovskite materials at  $T = 0$  K and  $P = 0$  GPa

References	Compound	$A$	$A^U$	$A^{\text{eq}}$	$A_G$	$A^B$
This work	$\text{TiPbO}_3$	0.670	1.886	1.483	0.125	0.183
	$\text{TiSnO}_3$	1.113	0.013	1.033	0.001	0
	$\text{ZrPbO}_3$	0.652	0.221	1.145	0.021	0
	$\text{ZrSnO}_3$	-0.767	-4.884	0.794	-0.954	0



offering unique insights into their suitability for advanced applications.  $\text{TiPbO}_3$  emerges as the most versatile compound, with an  $A$  value of 0.670 reflecting balanced stability and the

highest  $A^U$  value of 1.886, underscoring robust structural interactions. Its  $A^{\text{eq}}$  value of 1.483 highlights superior bonding capabilities, while consistent contributions from  $A_G$  at 0.125

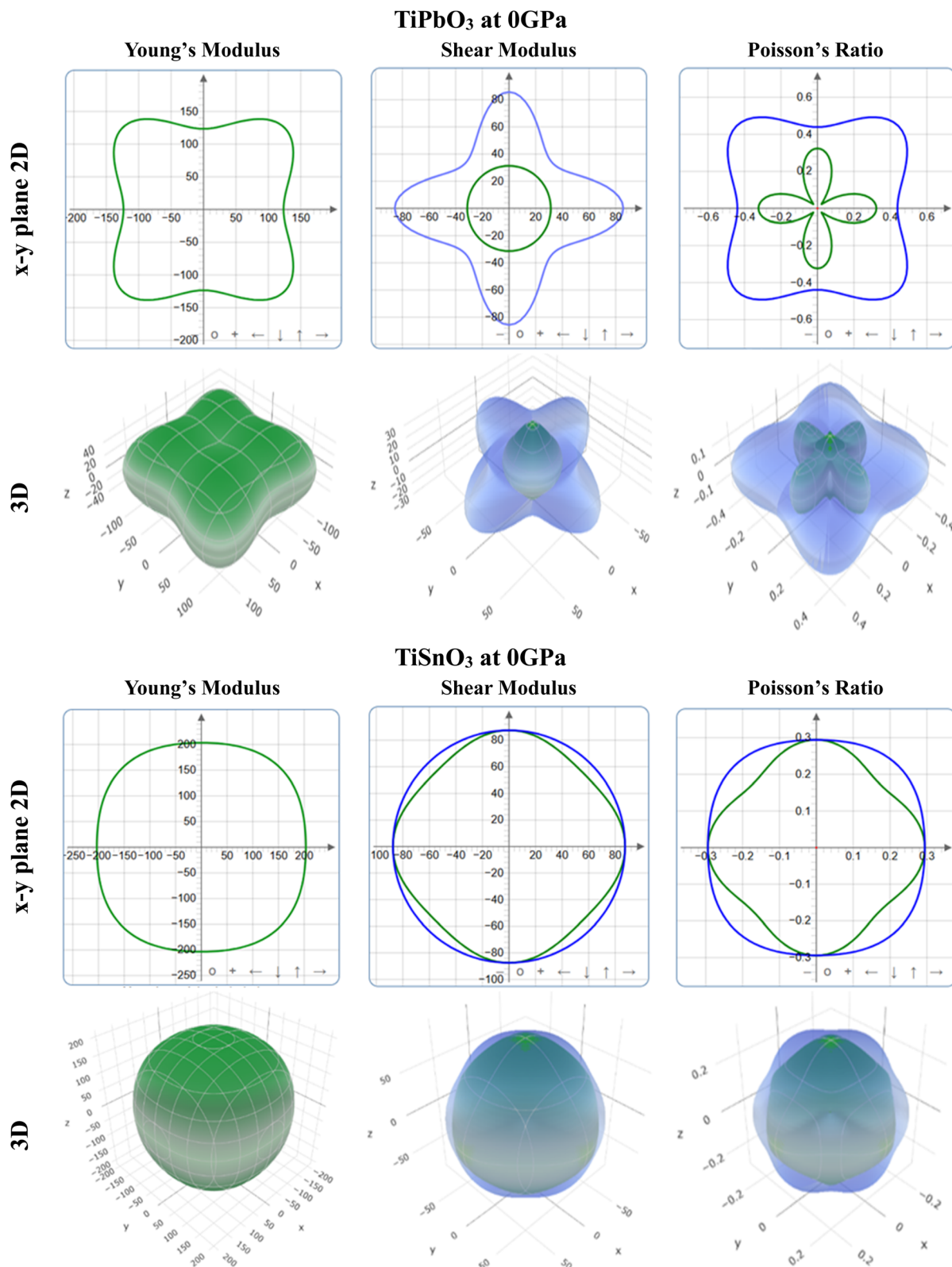


Fig. 9 Anisotropic 3D representation of Young's modulus, Shear modulus, and Poisson's ratio of  $\text{TiDO}_3$  perovskite materials.



and  $A^B$  at 0.183 make it a top candidate for multifunctional applications.  $\text{TiSnO}_3$  dominates in the  $A$  parameter with the highest value of 1.113, showcasing exceptional stability and positioning it as ideal for applications prioritizing structural resilience. However, its minimal contributions to  $A^U$ ,  $A_G$ , and  $A^B$  limit its versatility.  $\text{ZrPbO}_3$  offers stable but moderate performance, with an  $A$  value of 0.652 and an  $A^{\text{eq}}$  value of 1.145, making it well-suited for general-purpose applications where extreme performance is not required. Conversely,  $\text{ZrSnO}_3$  faces significant challenges, with negative  $A$ ,  $A^U$ , and  $A_G$  values indicating instability and diminished bonding strength. While its  $A^{\text{eq}}$  value of 0.794 is positive, it is the lowest among all compounds, and the absence of  $A^B$  contributions further narrows its potential. These findings highlight  $\text{TiPbO}_3$  as a robust and versatile option,  $\text{TiSnO}_3$  as a high-stability specialist,  $\text{ZrPbO}_3$  as a reliable all-rounder, and  $\text{ZrSnO}_3$  as a material requiring refinement. This analysis underscores the potential of  $\text{ZDO}_3$  perovskites (without  $\text{ZrSnO}_3$ ) for tailored applications in Solar cell device technologies, paving the way for future advancements.

### 3.8. Anisotropic properties

The provided figures illustrate the anisotropic mechanical properties, namely Young's modulus, shear modulus, and

Poisson's ratio of the  $\text{ZDO}_3$  compounds, excluding  $\text{ZrSnO}_3$ . The analyzed perovskite materials include  $\text{TiPbO}_3$ ,  $\text{TiSnO}_3$ , and  $\text{ZrPbO}_3$  at 0 GPa, with a focus on their directional dependence in mechanical behavior. These anisotropic properties were calculated using the ELATE tensor analysis tool implemented in Python, which enables precise visualization and interpretation of directional mechanical responses.<sup>60</sup> Among them,  $\text{TiPbO}_3$  exhibits pronounced anisotropy across all evaluated mechanical parameters. Fig. 9 and 10 present both two-dimensional and three-dimensional visualizations of Young's modulus, revealing directional stiffness variations and highlighting the sensitivity of this property to crystallographic orientation. Similarly, the shear modulus displays anisotropic features, with a lobed 2D contour and a flattened 3D surface, confirming non-uniform shear response. Poisson's ratio also shows directional variability, indicating that the material's expansion–contraction behavior depends on the direction of the applied stress. This inherent anisotropy in  $\text{TiPbO}_3$  suggests its potential for applications requiring directional mechanical control, such as piezoelectric devices and adaptive structural components.

On the other hand, we find that  $\text{TiSnO}_3$  exhibits near-isotropic characteristics to all the properties. The plots of Young's modulus and shear modulus are circular in 2D and isotropic in the 3D plane, indicating equal stiffness and equal

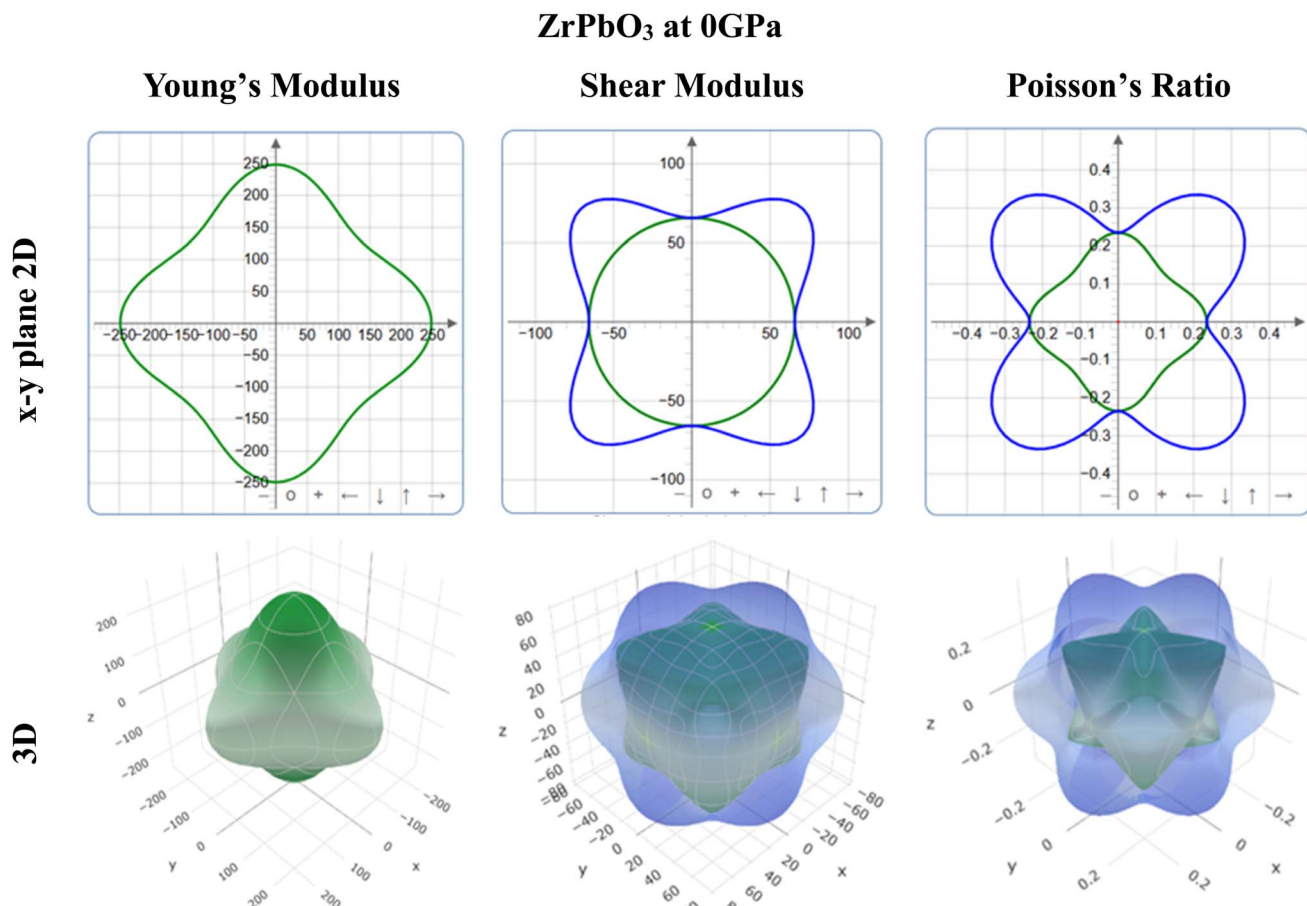


Fig. 10 Anisotropic 3D representation of Young's modulus, Shear modulus, Poisson's ratio of  $\text{ZrPbO}_3$  perovskite materials.



resistance to shear stress. Poisson's ratio exhibits mild anisotropy as well since its behavior essentially does not vary significantly across the orientations. These characteristics make  $\text{TiSnO}_3$  suitable for structural applications where a uniform mechanical response to multidirectional stress is desired. Specifically, the presented bulk material of  $\text{ZrPbO}_3$  has moderately anisotropic properties.

This gave Young's modulus directionality, and this has regions of higher stiffness corresponding to particular directionality. Like with the previous material, both the shear modulus and Poisson's ratio show anisotropic characteristics, although not as pronounced as those of the  $\text{TiPbO}_3$  material. The combination of isotropy and anisotropy properties of  $\text{ZrPbO}_3$  makes it suitable for hybrid applications where directional as well as omnidirectional properties are preferable, such as transducers or actuators.  $\text{TiPbO}_3$  possesses a high anisotropy for directionally specific application, while  $\text{TiSnO}_3$  exhibits a large isotropy for general structural application, and  $\text{ZrPbO}_3$  has moderate anisotropy, which can be useful for a combination of applications. These differences in elastic properties bring out the fact that these materials can be engineered to achieve the intended and desired engineering and functional characteristics.

### 3.9. Population analysis

Population analysis examines the charge present in specific atomic orbitals, providing insights into the electronic structure of materials. Mulliken atomic population describes the distribution of charge among atoms in a crystal lattice, highlighting their electronic interactions. Mulliken charge is calculated as the difference between the actual number of electrons in the outermost orbital and the expected number.<sup>61</sup> When the

Mulliken charge is positive, it suggests that the outermost orbital has fewer electrons than anticipated, indicating electron loss.<sup>62</sup> Conversely, a negative Mulliken charge reflects an excess of electrons in the orbital, signifying electron gain. These variations in electron count arise from electron transfer between atoms, shedding light on the nature of bonding and charge redistribution within the crystal. This analysis is crucial for understanding the electronic properties and behavior of complex materials. A comparative study to predict regioselectivity, electrophilicity, and nucleophilicity with Fukui function and Hirshfeld charge.<sup>63</sup> The  $\text{ZDO}_3$  perovskites ( $\text{Z} = \text{Ti}, \text{Zr}; \text{D} = \text{Pb}, \text{Sn}$ ) were rigorously analyzed for their physical, electronic, and charge distribution properties, revealing distinct trends in charge spilling, orbital contributions, and charge dynamics across  $\text{TiPbO}_3$ ,  $\text{TiSnO}_3$ ,  $\text{ZrPbO}_3$ , and  $\text{ZrSnO}_3$  in Table 5. The charge spilling values progressively increase from 0.14% in  $\text{TiPbO}_3$  to 0.19% in  $\text{TiSnO}_3$ , 0.20% in  $\text{ZrPbO}_3$ , and peak at 0.26% in  $\text{ZrSnO}_3$ , indicating that Zr- and Sn-based compounds exhibit greater charge redistribution and electronic activity compared to Ti- and Pb-based materials.  $\text{ZrSnO}_3$ , with the highest charge spillage, demonstrates the most significant charge redistribution, positioning it as a highly responsive material suitable for advanced optoelectronic and high-conductivity applications. The Mulliken atomic populations provide detailed insights into the orbital contributions of each compound. Oxygen atoms dominate the bonding framework across all compounds, with p orbital contributions increasing from 4.90 in  $\text{TiPbO}_3$ , 4.87 in  $\text{TiSnO}_3$ , and 4.95 in  $\text{ZrPbO}_3$ , reaching the highest value of 5.02 in  $\text{ZrSnO}_3$ . This highlights oxygen's critical role in fostering robust covalent bonding.

Ti atoms in  $\text{TiPbO}_3$  and  $\text{TiSnO}_3$  contribute significantly to bonding, with d orbital populations of 6.52 and 6.61, and total

Table 5 Mulliken and Hirshfeld charge analysis of different atoms of  $\text{ZDO}_3$  ( $\text{Z} = \text{Ti}, \text{Zr}$ , and  $\text{D} = \text{Pb}, \text{Sn}$ )

Compound	Change spilling	Species	Mulliken atomic populations					Milliken change	Hirshfeld change
			s	p	d	f	Total		
$\text{TiPbO}_3$	0.14%	0	1.88	4.79	0	0	6.67	-0.67	-0.33
		0	1.86	4.90	0	0	6.76	-0.76	-0.34
		0	1.86	4.90	0	0	6.76	-0.76	-0.34
		Ti	2.33	6.52	2.20	0	11.05	0.95	0.43
		Pb	3.77	6.99	10.00	0	20.77	1.23	0.57
$\text{TiSnO}_3$	0.19%	0	1.85	4.87	0	0	6.72	-0.72	-0.33
		0	1.85	4.87	0	0	6.72	-0.72	-0.33
		0	1.85	4.87	0	0	6.72	-0.72	-0.33
		Ti	2.40	6.61	2.17	0	11.18	0.82	0.39
		Sn	1.72	0.95	10.00	0	12.67	1.33	0.59
$\text{ZrPbO}_3$	0.20%	0	1.85	4.95	0	0	6.81	-0.81	-0.37
		0	1.85	4.95	0	0	6.81	-0.81	-0.37
		0	1.85	4.95	0	0	6.81	-0.81	-0.37
		Zr	2.43	6.56	1.99	00	10.98	1.02	0.41
		Pb	3.66	6.95	10.00	0	20.60	1.40	0.69
$\text{ZrSnO}_3$	0.26%	0	1.89	5.02	0	0	6.91	-0.91	-0.30
		0	1.89	5.02	0	0	6.91	-0.91	-0.30
		0	1.89	5.02	0	0	6.91	-0.91	-0.30
		Zr	2.55	6.45	2.50	0	11.49	0.51	0.36
		Sn	0.50	1.29	10.00	0	11.78	2.22	0.51



electron populations of 11.05 and 11.18, respectively. In contrast, Zr atoms in  $\text{ZrPbO}_3$  and  $\text{ZrSnO}_3$  show slightly reduced d orbital contributions of 6.56 and 6.45, corresponding to total populations of 10.98 and 11.49, reflecting subtle differences in their electronic behavior. Pb atoms in  $\text{TiPbO}_3$  and  $\text{ZrPbO}_3$  demonstrate strong p and d orbital contributions, with total populations of 20.77 and 20.60, while Sn atoms in  $\text{TiSnO}_3$  and  $\text{ZrSnO}_3$  dominate with p orbital contributions of 10.00, resulting in total populations of 12.67 and 11.78, underscoring Sn's vital role in enhancing metallic bonding, particularly in  $\text{ZrSnO}_3$ . The Mulliken and Hirshfeld charge analyses further reveal critical differences in charge distribution among the compounds. In  $\text{TiPbO}_3$ , Ti exhibits Mulliken and Hirshfeld charges of 0.95 and 0.43, respectively, while Pb shows charges of 1.23 and 0.57, reflecting balanced charge distributions with minimal polarization.  $\text{TiSnO}_3$  exhibits increased bonding activity, with Ti showing Mulliken and Hirshfeld charges of 0.82 and 0.39, while Sn demonstrates stronger bonding contributions with charges of 1.33 and 0.59.

In  $\text{ZrPbO}_3$ , Zr's Mulliken and Hirshfeld charges are 1.02 and 0.41, while Pb shows higher values of 1.40 and 0.69, indicating stronger bonding interactions.  $\text{ZrSnO}_3$  exhibits the highest charge redistribution, with Mulliken charges of 0.51 for Zr and 2.22 for Sn, and Hirshfeld charges of 0.36 and 0.51, reflecting its strong metallic bonding nature and enhanced electronic activity. Sn-containing materials exhibit higher charge redistribution and bonding activity compared to Pb-containing compounds, while Zr-based compounds show greater charge spilling than Ti-based materials. Oxygen atoms play a dominant

role in bonding, with their p orbitals contributing most significantly in  $\text{ZrSnO}_3$ , emphasizing its robust covalent bonding framework. Ti-based compounds, with their stable charge distributions, are well-suited for optoelectronic devices requiring predictability and reliability. In contrast, Zr-based compounds, particularly  $\text{ZrSnO}_3$ , excel in high charge redistribution and metallic bonding, making them ideal candidates for high-conductivity and advanced electronic applications. These findings provide a nuanced understanding of the interplay between charge distribution, orbital contributions, and electronic properties in ZDO<sub>3</sub> perovskites, paving the way for their application in mechanical technologies.

### 3.10. Phonon analysis

Phonon analysis examines the vibrational behavior of atoms in a crystal to determine a material's dynamic stability. The absence of imaginary frequencies confirms structural stability, while their presence signals possible lattice instabilities or phase transitions.<sup>64</sup> It also reveals crucial thermal and mechanical properties, influencing material performance in devices. This makes phonon analysis vital for designing stable materials in electronics, photovoltaics, and thermoelectric.

Fig. 11 presents the phonon dispersion curves for four perovskite compounds,  $\text{TiPbO}_3$ ,  $\text{TiSnO}_3$ ,  $\text{ZrPbO}_3$ , and  $\text{ZrSnO}_3$ , plotted along the high-symmetry points X-R-M- $\Gamma$ -R, with frequency (in THz) as a function of wave vector. In Fig. 11(a),  $\text{TiPbO}_3$  exhibits no imaginary frequencies, indicating dynamic stability. Its acoustic modes extend up to  $\sim$ 5 THz, while optical

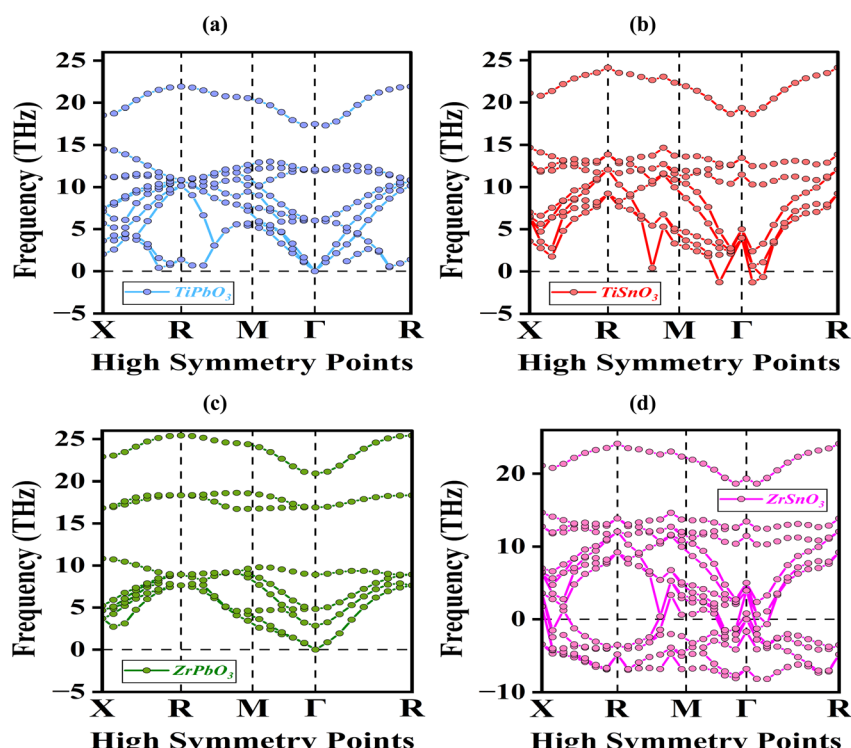


Fig. 11 Phonon dispersion curves of (a)  $\text{TiPbO}_3$ , (b)  $\text{TiSnO}_3$ , (c)  $\text{ZrPbO}_3$ , and (d)  $\text{ZrSnO}_3$  Perovskites along high-symmetry directions (X-R-M- $\Gamma$ -R).



modes reach 23.26 THz. In contrast, Fig. 11(b) shows that  $\text{TiSnO}_3$  has imaginary frequencies dipping to  $-2$  THz near the  $M$  and  $\Gamma$  points, suggesting dynamic instability, despite optical modes reaching similar frequencies.  $\text{ZrPbO}_3$ , shown in Fig. 11(c), is also dynamically stable, with phonon frequencies ranging from 0 to 22 THz. Its acoustic modes peak around 5 THz, and optical branches are well dispersed. However,  $\text{ZrSnO}_3$  in Fig. 11(d) displays pronounced dynamic instability, with deep imaginary frequencies down to  $-8$  THz and optical modes peaking between 21 and 22 THz. The presence of imaginary modes in  $\text{TiSnO}_3$  and especially  $\text{ZrSnO}_3$  indicates potential lattice distortions or phase transitions, rendering them unsuitable for stable device integration in their current crystalline form. In contrast, the absence of imaginary frequencies in  $\text{TiPbO}_3$  and  $\text{ZrPbO}_3$  confirms their dynamic stability, making them promising candidates for optoelectronic and thermoelectric applications where structural robustness is essential.

## 4 Conclusion

This study offers a comprehensive evaluation of  $\text{TiPbO}_3$ ,  $\text{TiSnO}_3$ ,  $\text{ZrPbO}_3$ , and  $\text{ZrSnO}_3$  perovskites, revealing significant variation in their structural, electronic, optical, and mechanical properties, each of which suggests distinct potential applications. Structurally, all compounds exhibit cubic perovskite symmetry and stable tolerance factors, with  $\text{ZrPbO}_3$  displaying the lowest formation energy, making it the most thermodynamically stable, a key requirement for long-term device reliability. Electronically,  $\text{ZrPbO}_3$  and  $\text{TiPbO}_3$  exhibit wide and moderate indirect band gaps, respectively, suggesting their suitability for UV photodetectors and visible-light photovoltaic devices.  $\text{TiSnO}_3$ , with its narrower band gap, is promising for thermoelectric and infrared optoelectronic applications, while the metallic  $\text{ZrSnO}_3$  may serve in conductive coatings or electrodes. Density of states (DOS) analysis confirms the semiconducting and metallic nature of these compounds, while charge density and population analyses reveal strong covalent bonding between metal–oxygen pairs and significant charge redistribution in Sn- and Zr-based systems, indicating favorable electronic mobility and reactivity, important for catalysis or sensing. Spin polarization studies show mild magnetic asymmetry, suggesting potential use in spintronic or magnetic devices, particularly for  $\text{TiPbO}_3$  and  $\text{ZrPbO}_3$ . Optical analyses reveal that  $\text{TiSnO}_3$  and  $\text{ZrPbO}_3$  offer excellent visible-light absorption, positioning them as ideal candidates for solar absorbers and photodetectors.  $\text{ZrSnO}_3$  stands out with high UV reflectivity and loss-function peaks in the high-energy range, indicating its potential for UV shielding and plasmonic applications. Mechanical property analysis indicates that  $\text{TiSnO}_3$  and  $\text{ZrPbO}_3$  are ductile and exhibit high stiffness and hardness, which is desirable for robust structural components in multi-functional devices. In contrast,  $\text{TiPbO}_3$ , though more brittle, shows high anisotropy, making it suitable for directional mechanical applications like piezoelectric sensors.  $\text{ZrSnO}_3$ , despite its high bulk modulus, exhibits negative shear values and dynamic instability, limiting its use without structural modifications. Anisotropy analyses using ELATE confirm that

$\text{TiPbO}_3$  is highly directionally sensitive, ideal for piezoelectric and stress-responsive materials, while  $\text{TiSnO}_3$ 's near-isotropic nature suits it for uniform structural applications.  $\text{ZrPbO}_3$ 's moderate anisotropy makes it a strong candidate for hybrid systems requiring both directional and uniform responses. Phonon dispersion results further validate the dynamic stability of  $\text{TiPbO}_3$  and  $\text{ZrPbO}_3$ , while  $\text{TiSnO}_3$  and  $\text{ZrSnO}_3$  show imaginary frequencies, hinting at possible phase transitions or instabilities that must be addressed before practical deployment. Finally,  $\text{TiPbO}_3$  and  $\text{ZrPbO}_3$  emerge as versatile and stable materials suitable for optoelectronic, photovoltaic, and mechanical applications.  $\text{TiSnO}_3$  shows promise in energy conversion and thermal applications due to its ductility and narrow band gap.  $\text{ZrSnO}_3$ , although dynamically unstable in its current form, may find niche roles in conductive and plasmonic devices after structural engineering. This application-driven insight bridges the gap between theoretical modeling and real-world device integration, guiding future experimental work.

## Ethical statement

The manuscript's authors agree that there is no research involving human participants, human data or tissue, or animal subjects.

## Author contributions

Md. Sakib Hasan Saikot, Rifat Rafiu, Imtiaz Ahamed Apon, Md. Azizur Rahman: methodology, validation, software, conceptualization, investigation, formal analysis, data curation, visualization, writing – original draft, and review and editing. Ali El-Rayyes, Mohd Shkir, Zubair Ahmad, R. Marnadu: investigation, validation, software, formal analysis, data curation, writing – original draft, and review and editing.

## Conflicts of interest

The authors have no conflicts of interest.

## Data availability

Data will be made available on reasonable request.

Supplementary information is available. See DOI: <https://doi.org/10.1039/d5ra06065f>.

## Acknowledgements

The authors extend their appreciation to University Higher Education Fund for funding this research work under Research Support Program for Central labs at King Khalid University through the project number CL/PRI/A/8.



## References

1 G. A. Samara, The relaxational properties of compositionally disordered  $\text{ABO}_3$  perovskites, *J. Phys.: Condens. Matter*, 2003, **15**, R367–R411, DOI: [10.1088/0953-8984/15/9/202](https://doi.org/10.1088/0953-8984/15/9/202).

2 J. E. Geusic, S. K. Kurtz, L. G. Van Uitert and S. H. Wemple, Electro-Optic Properties Of Some  $\text{Abo}_3$  Perovskites In The Paraelectric Phase, *Appl. Phys. Lett.*, 1964, **4**, 141–143, DOI: [10.1063/1.1754003](https://doi.org/10.1063/1.1754003).

3 R. Stumper, D. Wagner and D. Bäuerle, Influence of bulk and interface properties on the electric transport in  $\text{ABO}_3$  perovskites, *Phys. Status Solidi A*, 1983, **75**, 143–154, DOI: [10.1002/pssa.2210750116](https://doi.org/10.1002/pssa.2210750116).

4 Z.-K. Tan, R. S. Moghaddam, M. L. Lai, P. Docampo, R. Higler, F. Deschler, M. Price, A. Sadhanala, L. M. Pazos, D. Credgington, F. Hanusch, T. Bein, H. J. Snaith and R. H. Friend, Bright light-emitting diodes based on organometal halide perovskite, *Nat. Nanotechnol.*, 2014, **9**, 687–692, DOI: [10.1038/nnano.2014.149](https://doi.org/10.1038/nnano.2014.149).

5 K. Zhang, N. Zhu, M. Zhang, L. Wang and J. Xing, Opportunities and challenges in perovskite LED commercialization, *J. Mater. Chem. C*, 2021, **9**, 3795–3799, DOI: [10.1039/D1TC00232E](https://doi.org/10.1039/D1TC00232E).

6 R. L. Z. Hoye, J. Hidalgo, R. A. Jagt, J. Correa-Baena, T. Fix and J. L. MacManus-Driscoll, The Role of Dimensionality on the Optoelectronic Properties of Oxide and Halide Perovskites, and their Halide Derivatives, *Adv. Energy Mater.*, 2022, **12**, 2100499, DOI: [10.1002/aenm.202100499](https://doi.org/10.1002/aenm.202100499).

7 A. R. Chakhmouradian and P. M. Woodward, Celebrating 175 years of perovskite research: a tribute to Roger H. Mitchell, *Phys. Chem. Miner.*, 2014, **41**, 387–391, DOI: [10.1007/s00269-014-0678-9](https://doi.org/10.1007/s00269-014-0678-9).

8 L. Ortega-San-Martin, Correction to: Introduction to Perovskites: A Historical Perspective, in *Revolut. Perovskite*, ed. N. S. Arul, and V. D. Nithya, Springer Singapore, Singapore, 2020, pp. C1, DOI: [10.1007/978-981-15-1267-4\\_12](https://doi.org/10.1007/978-981-15-1267-4_12).

9 A. Von Hippel, R. G. Breckenridge, F. G. Chesley and L. Tisza, High dielectric constant ceramics, *Ind. Eng. Chem.*, 1946, **38**, 1097–1109, DOI: [10.1021/ie50443a009](https://doi.org/10.1021/ie50443a009).

10 S. A. Rouf, M. I. Hussain, U. Mumtaz, A. M. Majeed and H. T. Masood, A density functional theory study of the structural, electronic, and optical properties of  $\text{XGaO}_3$  ( $\text{X} = \text{V, Nb}$ ) perovskites for optoelectronic applications, *J. Comput. Electron.*, 2021, **20**, 1484–1495, DOI: [10.1007/s10825-021-01718-3](https://doi.org/10.1007/s10825-021-01718-3).

11 M. I. Hussain, R. M. Arif Khalil, F. Hussain, A. M. Rana, G. Murtaza and M. Imran, Probing the structural, electronic, mechanical strength and optical properties of tantalum-based oxide perovskites  $\text{ATaO}_3$  ( $\text{A} = \text{Rb, Fr}$ ) for optoelectronic applications: First-principles investigations, *Optik*, 2020, **219**, 165027, DOI: [10.1016/j.ijleo.2020.165027](https://doi.org/10.1016/j.ijleo.2020.165027).

12 M. F. M. Taib, N. H. Hussin, M. H. Samat, O. H. Hassan and M. Z. A. Yahya, Structural, Electronic and Optical Properties of  $\text{BaTiO}_3$  and  $\text{BaFeO}_3$  From First Principles LDA+U Study, *Int. J. Electroact. Mater.*, 2016, **4**, 14–17.

13 H.-R. Liu, J.-H. Yang, H. J. Xiang, X. G. Gong and S.-H. Wei, Origin of the superior conductivity of perovskite  $\text{Ba}(\text{Sr})\text{SnO}_3$ , *Appl. Phys. Lett.*, 2013, **102**, 112109, DOI: [10.1063/1.4798325](https://doi.org/10.1063/1.4798325).

14 M. Yaseen, A. Ashfaq, A. Akhtar, R. Asghar, H. Ambreen, M. K. Butt, S. Noreen, S. Ur Rehman, S. Bibi, S. M. Ramay and A. Murtaza, Investigation of  $\text{LaAlO}_3$  pervoskite compound for optoelectronic and thermoelectric devices under pressure, *Mater. Res. Express*, 2020, **7**, 015907, DOI: [10.1088/2053-1591/ab6110](https://doi.org/10.1088/2053-1591/ab6110).

15 K. E. Babu, N. Murali, K. V. Babu, P. T. Shibeshi, and V. Veeraiah, Investigation of optoelectronic properties of cubic perovskite  $\text{LaGaO}_3$ , in *NIT, CALICUT, Kerala, India 673 601*, 2014, pp. 173–178, DOI: [10.1063/1.4898236](https://doi.org/10.1063/1.4898236).

16 M. K. Yaakob, M. H. Ridzwan, M. F. M. Taib, L. Li, O. H. Hassan and M. Z. A. Yahya, First-principles investigation of the ground state, structural phase transition, and magnetic ordering of strained  $\text{BiVO}_3$ , *J. Appl. Phys.*, 2019, **125**, 082532, DOI: [10.1063/1.5053942](https://doi.org/10.1063/1.5053942).

17 C. E. Ekuma, M. Jarrell, J. Moreno and D. Bagayoko, First principle electronic, structural, elastic, and optical properties of strontium titanate, *AIP Adv.*, 2012, **2**(1), 012189, DOI: [10.1063/1.3700433](https://doi.org/10.1063/1.3700433).

18 M. L. Ali and M. Z. Rahaman, The Structural, Elastic, Electronic and Optical Properties of Cubic Perovskite  $\text{SrVO}_3$  Compound: An *Ab Initio* Study, *Int. J. Mater. Sci. Appl.*, 2016, **5**(5), 202–206, DOI: [10.11648/j.ijmsa.20160505.14](https://doi.org/10.11648/j.ijmsa.20160505.14).

19 K. M. Hossain, M. H. K. Rubel, M. M. Rahaman, M. M. Hossain, M. I. Hossain, A. A. Khatun, J. Hossain, and A. K. M. A. Islam, A comparative theoretical study on physical properties of synthesized  $\text{AVO}_3$  ( $\text{A} = \text{Ba, Sr, Ca, Pb}$ ) perovskites, *arXiv*, 2019, preprint, arXiv:1905.01437, DOI: [10.48550/ARXIV.1905.01437](https://doi.org/10.48550/ARXIV.1905.01437).

20 S. A. Khandy and D. C. Gupta, Investigation of structural, magneto-electronic, and thermoelectric response of ductile  $\text{SnAlO}_3$  from high-throughput DFT calculations, *Int. J. Quantum Chem.*, 2017, **117**, e25351, DOI: [10.1002/qua.25351](https://doi.org/10.1002/qua.25351).

21 M. Roknuzzaman, K. Ostrikov, H. Wang, A. Du and T. Tesfamichael, Towards lead-free perovskite photovoltaics and optoelectronics by ab-initio simulations, *Sci. Rep.*, 2017, **7**, 14025, DOI: [10.1038/s41598-017-13172-y](https://doi.org/10.1038/s41598-017-13172-y).

22 M. Musa Saad H.-E., Promising half-metallic ferromagnetism in double perovskites  $\text{Ba}_2\text{VTO}_6$  ( $\text{T}=\text{Nb}$  and  $\text{Mo}$ ): *ab initio* LMTO-ASA investigations, *Solid State Commun.*, 2012, **152**, 1230–1233.

23 H. Wang, H. Huang and B. Wang, First-principles study of structural, electronic, and optical properties of, *Solid State Commun.*, 2009, **149**, 1849–1852, DOI: [10.1016/j.ssc.2009.07.009](https://doi.org/10.1016/j.ssc.2009.07.009).

24 S. Kuma and M. M. Woldemariam, Structural, Electronic, Lattice Dynamic, and Elastic Properties of  $\text{SnTiO}_3$  and  $\text{PbTiO}_3$  Using Density Functional Theory, *Adv. Condens. Matter Phys.*, 2019, **2019**, 1–12, DOI: [10.1155/2019/3176148](https://doi.org/10.1155/2019/3176148).

25 S. Rahman, A. Hussain, S. Noreen, N. Bibi, S. Arshad, J. U. Rehman and M. B. Tahir, Structural, electronic, optical and mechanical properties of oxide-based perovskite  $\text{ABO}_3$  ( $\text{A} = \text{Cu, Nd}$  and  $\text{B} = \text{Sn, Sc}$ ): A DFT



study, *J. Solid State Chem.*, 2023, **317**, 123650, DOI: [10.1016/j.jssc.2022.123650](https://doi.org/10.1016/j.jssc.2022.123650).

26 M. F. M. Taib, M. K. Yaakob, A. Chandra, A. K. M. Arof and M. Z. A. Yahya, Effect of Pressure on Structural, Electronic and Elastic Properties of Cubic (Pm3m)  $\text{SnTiO}_3$  Using First Principle Calculation, *Adv. Mater. Res.*, 2012, **501**, 342–346, DOI: [10.4028/www.scientific.net/AMR.501.342](https://doi.org/10.4028/www.scientific.net/AMR.501.342).

27 M. D. Segall, P. J. D. Lindan, M. J. Probert, C. J. Pickard, P. J. Hasnip, S. J. Clark and M. C. Payne, First-principles simulation: ideas, illustrations and the CASTEP code, *J. Phys.: Condens. Matter*, 2002, **14**, 2717–2744, DOI: [10.1088/0953-8984/14/11/301](https://doi.org/10.1088/0953-8984/14/11/301).

28 J. P. Perdew, K. Burke and M. Ernzerhof, Generalized Gradient Approximation Made Simple, *Phys. Rev. Lett.*, 1996, **77**, 3865–3868, DOI: [10.1103/PhysRevLett.77.3865](https://doi.org/10.1103/PhysRevLett.77.3865).

29 M. M. Saad H.-E and A. Elhag, DFT study on the crystal, electronic and magnetic structures of tantalum based double perovskite oxides  $\text{Ba}_2\text{MTaO}_6$  (M = Cr, Mn, Fe) via GGA and GGA + U, *Results Phys.*, 2018, **9**, 793–805, DOI: [10.1016/j.rinp.2018.03.055](https://doi.org/10.1016/j.rinp.2018.03.055).

30 Y.-M. Juan, E. Kaxiras and R. G. Gordon, Use of the generalized gradient approximation in pseudopotential calculations of solids, *Phys. Rev. B: Condens. Matter Mater. Phys.*, 1995, **51**, 9521–9525, DOI: [10.1103/PhysRevB.51.9521](https://doi.org/10.1103/PhysRevB.51.9521).

31 S. Idrissi, A. Jabar and L. Bahmad, Origin of semiconductor and half-metallic behaviors in the perovskite materials  $\text{Rb}_2\text{XF}_3$  (X = Co, Mn, Fe or V): A GGA + U approach, *Int. J. Quantum Chem.*, 2024, **124**, e27341, DOI: [10.1002/qua.27341](https://doi.org/10.1002/qua.27341).

32 M. Riaz, M. S. U. Sahar, S. M. Ali, M. F. Shah, S. M. J. Zaidi and M. I. Khan, Investigation of stress-induced effects on structural, optoelectronic, and elastic characteristics of cubic  $\text{CaHfO}_3$  perovskite oxide; A DFT study, *Comput. Condens. Matter*, 2023, **37**, e00846, DOI: [10.1016/j.cocom.2023.e00846](https://doi.org/10.1016/j.cocom.2023.e00846).

33 H. J. Monkhorst and J. D. Pack, Special points for Brillouin-zone integrations, *Phys. Rev. B*, 1976, **13**, 5188–5192, DOI: [10.1103/PhysRevB.13.5188](https://doi.org/10.1103/PhysRevB.13.5188).

34 I. A. Apon, S. Jubayer, R. Boudissa, R. Kawsar, R. Rafiu, M. S. Refat, Md. S. H. Saikot, A. M. Alsuhaihani, Md. A. Rahman, Md. A. Hossain and N. Elboughdiri, Exploring  $\text{ACdX}_3$  Perovskites: DFT Analysis of Stability, Electronic, Optical, and Mechanical Properties for Solar Applications, *J. Inorg. Organomet. Polym. Mater.*, 2025, DOI: [10.1007/s10904-025-03821-5](https://doi.org/10.1007/s10904-025-03821-5).

35 Md. R. Hasan, I. A. Apon, Md. M. Islam, A. U. Azad, Md. Aminuzzman and Md. S. Haque, DFT based analysis of pressure driven mechanical, opto-electronic, and thermoelectric properties in lead-free  $\text{InGeX}_3$  (X = Cl, Br) perovskites for solar energy applications, *AIP Adv.*, 2024, **14**, 115109, DOI: [10.1063/5.0233863](https://doi.org/10.1063/5.0233863).

36 S. Rahman, A. Hussain, S. Noreen, N. Bibi, S. Arshad, J. U. Rehman and M. B. Tahir, Structural, electronic, optical and mechanical properties of oxide-based perovskite  $\text{ABO}_3$  (A = Cu, Nd and B = Sn, Sc): A DFT study, *J. Solid State Chem.*, 2023, **317**, 123650, DOI: [10.1016/j.jssc.2022.123650](https://doi.org/10.1016/j.jssc.2022.123650).

37 N. Bibi and M. Usman, Ruyhan, A theoretical investigation of  $\text{ABO}_3$  (A=Na and B = Ti, In) perovskites for solar cell and optoelectronic applications, *Mater. Sci. Semicond. Process.*, 2025, **186**, 109047, DOI: [10.1016/j.mssp.2024.109047](https://doi.org/10.1016/j.mssp.2024.109047).

38 A. M. Nura, S. R. Haladu, A. S. Gidado, L. Abubakar and R. S. Abraham, Determination of Structural, Electronic, and Elastic Properties of  $\text{SnTiO}_3$  using Density Functional Theory, *Phys. Access*, 2024, **04**, 17–23, DOI: [10.47514/phyaccess.2024.4.2.002](https://doi.org/10.47514/phyaccess.2024.4.2.002).

39 M. I. Khan, S. M. Junaid Zaidi, S. U. Sahar, S. M. Ali, M. Shahid and K. F. Fawy, Exploring the Hydrostatic Stress Effects on the Mechanical, Electronic, Thermal, and Optical Characteristics of Cubic  $\text{ThBeO}_3$ , *J. Inorg. Organomet. Polym. Mater.*, 2024, **35**(1), 641–650, DOI: [10.1007/s10904-024-03319-6](https://doi.org/10.1007/s10904-024-03319-6).

40 M. Z. Rahman, S. S. Hasan, M. S. Akter, N. M. Mukhtar, N. Absar, M. A. Hasan, T. Ichibha, R. Maezono, K. Hongo and M. A. Islam, Computational study of the structural, mechanical, electronic, optical and thermal properties of  $\text{BaLiX}$  (X =P, As, Sb) perovskites, *Phys. B*, 2024, **692**, 416387, DOI: [10.1016/j.physb.2024.416387](https://doi.org/10.1016/j.physb.2024.416387).

41 I. Y. Siddique, R. Khan, N. Rahman, S. Alshehri, M. D. Alshahrani, W. M. Almalki, V. Tirth, A. Algahtani, M. Husain, Nazish and A. Khan, Theoretical analysis of structural, electronic, optical, elastic and thermoelectric properties of double perovskites  $\text{Cs}_2\text{CuBiX}_6$  (X=Br or I): DFT approach, *Phys. B*, 2025, **715**, 417588, DOI: [10.1016/j.physb.2025.417588](https://doi.org/10.1016/j.physb.2025.417588).

42 A. A. Hassan, M. S. I. Ria, A. Ghosh, H. A. Alrafai, A. Al Baki, S. Khalaf Alla Abdelrahim, J. Y. Al-Humaidi, R. Islam Chowdhury Robin, M. M. Rahman and Md. Maniruzzaman, Investigating the physical characteristics and photovoltaic performance of inorganic  $\text{Ba}_3\text{NCl}_3$  perovskite utilizing DFT and SCAPS-1D simulations, *Mater. Sci. Eng., B*, 2024, **308**, 117559, DOI: [10.1016/j.mseb.2024.117559](https://doi.org/10.1016/j.mseb.2024.117559).

43 M. M. Haque, A. I. Shimul, A. Ghosh, N. S. Awwad and A. R. Chaudhry, Investigation of pressure-driven band gap variation and the physical characteristics of  $\text{Ba}_3\text{SbX}_3$  (X = F, Cl) perovskite for potential optoelectronic applications, *Opt. Express*, 2025, **33**, 30486–30504, DOI: [10.1364/OE.566477](https://doi.org/10.1364/OE.566477).

44 A. I. Shimul, S. R. Sarker, A. Ghosh, M. T. uz Zaman, H. A. Alrafai and A. A. Hassan, Examining the optoelectronic and photovoltaic characteristics of  $\text{Mg}_3\text{SbM}_3$  (M = F, Cl, Br) perovskites with diverse charge transport layers through numerical optimization and machine learning techniques, *Inorg. Chem. Commun.*, 2025, **179**, 114737, DOI: [10.1016/j.inoche.2025.114737](https://doi.org/10.1016/j.inoche.2025.114737).

45 Z. Ullah, B. Gul, A. S. Mohamed, A. Ali, G. Khan, M. S. Khan and F. Abbas, Spin-polarized electronic, optical, and transport properties of novel  $\text{Cs}_2\text{XMoBr}_6$  (X=Na, Li) HDPs: First-principles study, *Chem. Phys. Lett.*, 2024, **850**, 141471, DOI: [10.1016/j.cplett.2024.141471](https://doi.org/10.1016/j.cplett.2024.141471).

46 A. Kumar, A. Kumar and N. Iram, First-principles calculations to investigate structural, electronic, mechanical and optical properties of  $\text{SrAlO}_3$  compound,



Hybrid Adv., 2024, **6**, 100211, DOI: [10.1016/j.hybadv.2024.100211](https://doi.org/10.1016/j.hybadv.2024.100211).

47 W. Khan, S. B. Betzler, O. Šipr, J. Ciston, P. Blaha, C. Scheu and J. Minar, Theoretical and Experimental Study on the Optoelectronic Properties of Nb<sub>3</sub>O<sub>7</sub>(OH) and Nb<sub>2</sub>O<sub>5</sub> Photoelectrodes, *J. Phys. Chem. C*, 2016, **120**, 23329–23338, DOI: [10.1021/acs.jpcc.6b06391](https://doi.org/10.1021/acs.jpcc.6b06391).

48 U. K. Chowdhury, A. Rahman, A. Rahman, P. K. Das, M. U. Salma, S. Ali and D. C. Roy, The physical properties of ThCr<sub>2</sub>Si<sub>2</sub>-type Ru-based compounds SrRu<sub>2</sub>X<sub>2</sub> (X = P, Ge, As): An ab-initio investigation, *Phys. C*, 2019, **562**, 48–55, DOI: [10.1016/j.physc.2018.11.002](https://doi.org/10.1016/j.physc.2018.11.002).

49 M. A. Khatun, M. H. Mia, M. A. Hossain, F. Parvin and A. K. M. A. Islam, Optical and thermoelectric properties of layer structured Ba<sub>2</sub>X<sub>5</sub> (X = Zr, Hf) for energy harvesting applications, *J. Phys. Chem. Solids*, 2025, **196**, 112381, DOI: [10.1016/j.jpcs.2024.112381](https://doi.org/10.1016/j.jpcs.2024.112381).

50 C. Dong, X. Guan, Z. Wang, H. Zhao, Y. Kuai, S. Gao, C. Chen, W. Zou and P. Lu, The effects of cation and halide anion on the stability, electronic and optical properties of double perovskite Cs<sub>2</sub>NaMX<sub>6</sub> (M = In, Tl, Sb, bi; X = Cl, Br, I), *Comput. Mater. Sci.*, 2023, **220**, 112058, DOI: [10.1016/j.commatsci.2023.112058](https://doi.org/10.1016/j.commatsci.2023.112058).

51 A. Bouhemadou, R. Khenata, M. Chegaar and S. Maabed, First-principles calculations of structural, elastic, electronic and optical properties of the antiperovskite AsNMg<sub>3</sub>, *Phys. Lett. A*, 2007, **371**, 337–343, DOI: [10.1016/j.physleta.2007.06.030](https://doi.org/10.1016/j.physleta.2007.06.030).

52 M. Afsari, A. Boochani and M. Hantezadeh, Electronic, optical and elastic properties of cubic perovskite CsPbI<sub>3</sub>: Using first principles study, *Optik*, 2016, **127**, 11433–11443, DOI: [10.1016/j.ijleo.2016.09.013](https://doi.org/10.1016/j.ijleo.2016.09.013).

53 D. Behera, M. Manzoor, R. Sharma, M. M. Salah, I. Stich and S. K. Mukherjee, A Comprehensive First-Principles Investigation of SnTiO<sub>3</sub> Perovskite for Optoelectronic and Thermoelectric Applications, *Crystals*, 2023, **13**, 408, DOI: [10.3390/cryst13030408](https://doi.org/10.3390/cryst13030408).

54 W. Ullah, N. Rahman, M. Husain, W. M. Almalki, K. M. Abualnaja, G. Alosaimi, S. Belhachi, B. M. Al-Khamiseh, V. Tirth, A. Azzouz-Rached, H. A. Althobaiti and F. Ali, Modelling of structural, mechanical, electronic, and optical properties of Rb<sub>2</sub>TlXF<sub>6</sub> (X = Ir, Rh) double perovskite compounds through density functional theory, *Results Phys.*, 2025, **68**, 108079, DOI: [10.1016/j.rinp.2024.108079](https://doi.org/10.1016/j.rinp.2024.108079).

55 C. Dai, A. Wu, Y. Qi, Z. Chen and B. Li, Mechanical Properties of Paste Slurry under Constant Shear Rate in Initial Structure Failure Process, *Adv. Mater. Sci. Eng.*, 2019, **2019**, 2971563, DOI: [10.1155/2019/2971563](https://doi.org/10.1155/2019/2971563).

56 M. Jamal, S. Jalali Asadabadi, I. Ahmad and H. A. Rahnamaye Aliabad, Elastic constants of cubic crystals, *Comput. Mater. Sci.*, 2014, **95**, 592–599, DOI: [10.1016/j.commatsci.2014.08.027](https://doi.org/10.1016/j.commatsci.2014.08.027).

57 S. Rahman, A. Hussain, S. Noreen, N. Bibi, S. Arshad, J. U. Rehman and M. B. Tahir, Structural, electronic, optical and mechanical properties of oxide-based perovskite ABO<sub>3</sub> (A = Cu, Nd and B = Sn, Sc): A DFT study, *J. Solid State Chem.*, 2023, **317**, 123650, DOI: [10.1016/j.jssc.2022.123650](https://doi.org/10.1016/j.jssc.2022.123650).

58 M. Jamal, S. Jalali Asadabadi, I. Ahmad and H. A. Rahnamaye Aliabad, Elastic constants of cubic crystals, *Comput. Mater. Sci.*, 2014, **95**, 592–599, DOI: [10.1016/j.commatsci.2014.08.027](https://doi.org/10.1016/j.commatsci.2014.08.027).

59 P. S. Spoor, J. D. Maynard, M. J. Pan, D. J. Green, J. R. Hellmann and T. Tanaka, Elastic constants and crystal anisotropy of titanium diboride, *Appl. Phys. Lett.*, 1997, **70**, 1959–1961, DOI: [10.1063/1.118791](https://doi.org/10.1063/1.118791).

60 R. Gaillac, P. Pullumbi and F.-X. Couder, ELATE: an open-source online application for analysis and visualization of elastic tensors, *J. Phys.: Condens. Matter*, 2016, **28**, 275201, DOI: [10.1088/0953-8984/28/27/275201](https://doi.org/10.1088/0953-8984/28/27/275201).

61 B. Wang, C. Rong, P. K. Chattaraj and S. Liu, A comparative study to predict regioselectivity, electrophilicity and nucleophilicity with Fukui function and Hirshfeld charge, *Theor. Chem. Acc.*, 2019, **138**, 124, DOI: [10.1007/s00214-019-2515-1](https://doi.org/10.1007/s00214-019-2515-1).

62 M.-H. Lv, C.-M. Li and W.-F. Sun, Spin-Orbit Coupling and Spin-Polarized Electronic Structures of Janus Vanadium-Dichalcogenide Monolayers: First-Principles Calculations, *Nanomaterials*, 2022, **12**, 382, DOI: [10.3390/nano12030382](https://doi.org/10.3390/nano12030382).

63 S. Liu, Quantifying Reactivity for Electrophilic Aromatic Substitution Reactions with Hirshfeld Charge, *J. Phys. Chem. A*, 2015, **119**, 3107–3111, DOI: [10.1021/acs.jpcsa.5b00443](https://doi.org/10.1021/acs.jpcsa.5b00443).

64 M. Lawson, I. Williamson, Z.-Y. Ong and L. Li, First-principles analysis of structural stability, electronic and phonon transport properties of lateral MoS<sub>2</sub>-WX<sub>2</sub> heterostructures, *Comput. Condens. Matter*, 2019, **19**, e00389, DOI: [10.1016/j.cocom.2019.e00389](https://doi.org/10.1016/j.cocom.2019.e00389).

